We are IntechOpen,
the world's leading publisher of
Open Access books
Built by scientists, for scientists

4,800
Open access books available

122,000
International authors and editors

135M
Downloads

154
Countries delivered to

Our authors are among the

TOP 1%
most cited scientists

12.2%
Contributors from top 500 universities

BOOK CITATION INDEX — CLARIVATE ANALYTICS — INDEXED

WEB OF SCIENCE™

Selection of our books indexed in the Book Citation Index
in Web of Science™ Core Collection (BKCI)

Interested in publishing with us?
Contact book.department@intechopen.com

Investigations on Jet Footprint Geometry and its Characteristics for Complex Shape Machining with Abrasive Waterjets in Silicon Carbide Ceramic Material

S. Srinivasu D. and A. Axinte D.
University of Nottingham
United Kingdom

1. Introduction

Due to a combination of desirable mechanical properties, such as high hardness, wear resistance, strength at elevated temperatures in addition to corrosion resistance, chemical inertness, electromagnetic response and bio-compatibility, advanced ceramics are widely used for the manufacture of components for the optical, electronic, mechanical and biological industries (Siores et al., 1996; Chen et al., 1996). Silicon carbide (SiC), a structural ceramic, is increasingly being used for highly demanding engineering applications (bearings, valves, rotors, cutting tools, face seals, textile thread guides) where close dimensional/geometrical tolerances are required (Kahlmana, 2001). Furthermore, due to its low coefficient of thermal expansion, high thermal conductivity, high decomposition temperature, chemical inertness, low wettability by molten metal and low density, SiC is commonly used for heat resistant parts and refractory applications (Lee & Rainforth, 1992; Inasaki, 1987).

Although advanced ceramic components can be fabricated to net shape through hot-isostatic-pressing (HIP), a highly expensive process, final machining cannot be avoided to generate intricate surfaces and to meet the required quality specifications - dimensional accuracy, surface finish, elimination of surface flaws, as HIP is not economical for all applications (Richerson, 2006). In general, machining of ceramic components is usually done in the green state. However, to maintain dimensional control and production optimization, post-sintering machining unavoidable (Hocheng & Chang, 1994). On the other hand, milling of 3D surfaces is challenging with conventional machining approaches due to (i) component high hardness, which lead to excessive tool wear (ii) low fracture toughness of the workpiece materials, which lead to part fracture under the local machining forces (Chen et al., 1996; Hocheng & Chang, 1994). Diamond cutting (e.g. drilling)/grinding are commonly adopted for generating 3D features in sintered ceramics (Samant & Dahotre, 2009; Tuersley et al., 1994). However, conventional machining approaches might not always

be suitable as they demand dedicated tooling/fixtures to generate 3D features in such difficult-to-cut materials with the associated high cost and extended lead times.

As the machining often represents a significant portion of the fabrication cost of the final ceramic components, technologies suitable for cost effective machining of brittle materials (e.g. SiC) have to be identified. Various non-conventional approaches for machining of ceramics, such as ultrasonic, abrasive water jet (AWJ), electrical discharge and laser applications are reported and the trade-off between the material removal rate and the level of near-surface damage that these processes induce have been detailed (Samant & Dahotre, 2009; Tuersley et al., 1994). Among the non-conventional machining approaches, AWJ is a well utilized approach for machining hard to machine materials, such as ceramics at high material removal rate (MRR), with the advantage of reducing the above mentioned drawbacks of the conventional machining approaches (Chen et al., 1996; Kahlmana et al., 2001; Hashish, 1987; Chen et al., 1998). Furthermore, AWJs are suitable for machining of a wide range of materials due to its unique features, such as exertion of low cutting forces (<10N) at the machining zone, omni-directional cutting capability and material removal by micro cutting by abrasive particles, which eliminates the problem of chipping and fracture of brittle workpiece and leaving no heat affected zone (Zeng & Kim, 1996). A considerable amount of work has been reported on machining of ceramics with AWJs (Chen et al., 1996; Chen et al., 1998; Zeng et al., 1997; Hocheng & Chang, 1994; Gudimetla et al., 2002; Momber et al., 1996; Momber & Kovacevic, 2003; Zeng & Kim, 1996).

Freist et al. (1989) introduced the concept of 3D machining with AWJs. The concept is to break up the desired geometry into several parts and achieve each by the kerf shape generated by AWJs. The kerf geometry is described mathematically by a cosine function; however, milling is not demonstrated. There have been very limited efforts in the direction of controlled 3D complex shape generation with AWJs (Andrews & Horsfield, 1983). Ramp surface generation has been reported in X5CrNi189 material achieved by multi-pass linear-traverse milling in which the superposition of several kerfs is exploited as a strategy. A multi stage concentric pocket, 3D geometry, in a WC-Co hard metal is milled by the discrete milling approach proposed by Ojmertz. In milling of complex parts in advanced engineering materials (AEM), it is believed by the authors that jet footprints (JFP) with different shapes and dimensional characteristics (e.g. slopes equal to the local slope of the desired 3D complex geometry) have to be generated to approximate the local geometry of the desired complex part with the geometry of the suitable JFP. The JFPs with desired features can be realised by varying the jet feed rates and jet impingement angles, i.e. the angle between the jet axis and the target surface. Hence, complex 3D shapes in AEMs can be realised by AWJs, mainly, in two methods by: (i) varying the jet feed rate, and (ii) varying the jet impingement angle. In 2-axis and 5-axis AWJ milling of pockets, the bulk material in the targeted region is removed by raster scanning the surface by the jet (Ojmertz, 1997; Ojmertz & Amini, 1994; Laurinat et al., 2004). In 2-axis machining, the desired shape of the final component can be achieved by approximating the local geometry of the final complex 3D shape with the JFP characteristics generated at various jet feed rates at normal jet impingement angle. On the other hand, in complex shape generation by 5-axis machining, the jet is continuously manoeuvred, by varying the jet impingement angle, according to the local geometry of the

final complex shape - to match the JFP at that specific orientation with the local geometry of the desired part to be manufactured (Srinivasu et al., 2009).

In order to generate the controlled 3D complex shapes in AEMs, the variation in geometrical and dimensional characteristics (erosion depth (h), top width (w_t), slope of the side walls) of the jet footprint (JFP), which is the building block of the AWJ milling, with the variation in jet feed rate and jet impingement angle have to be known apriori (Miller, 2004; Srinivasu et al., 2009). Among them, the w_t is a critical measure that dictates the degree of the overlap to be employed, which influences the flatness of the bottom surface, depth of the pocket, surface roughness and longitudinal dimensions of the part, i.e. length and width (Ojmertz, 1997; Miller, 2004). Similarly, in profiling, drilling and slotting of hard to machine materials by macro/micro AWJs, the machined dimensions (e.g. diameter of hole) depend on the top width of the JFP. Freist et al. (1989) emphasised the need to study the JFP and its variation with the change in operating parameters, such as pump pressure (P), abrasive flow rate (m_f), jet feed rate (v), focusing nozzle diameter (d_f) and standoff distance (SOD), i.e. the axial distance between the tip of focusing nozzle and target material to be exposed to the jet. The characteristics of the JFP, such as erosion depth (h(α)), slope of the side walls, top width ($w_t(\alpha)$) depend on the d_f, φ (as in 2-axis machining); and SOD, which is influenced by α, and the jet impingement angle (Shipway, 1997). Hence, the w_t (α) has to be known at different α by considering the φ for controlled milling of complex shapes. Zeng et al. (1997) performed an experimental investigation to identify the optimal operating parameters and their influence on performance measures, such as depth of penetration, surface roughness and MRR in AWJ milling of alumina ceramics. In this study, d_f, lateral feed between passes, and SOD were found to be of critical importance in controlling the kerf geometry. Laurinat et al. (1993) and Freist et al. (1989) described the kerf geometry at both single pass and following multi-passes with different degrees of overlap by employing cosine function in hardened, austenitic and ferritic steels by varying operating parameters, such as P, d_f, m_f and v. The quality of the pockets with flat surfaces in terms of variation in depth of penetration and surface texture are analyzed by considering lateral feed, m_f, v, P and SOD (Ojmertz et al. (1997), Freist et al. (1989) and Laurinat et al. (1993)). It must be noted that despite different approaches up to now, only the generation of flat pockets have been achieved; the challenge of identifying methods to generate truly 3D surfaces still exists. Hashish (1993) has studied the influence of jet impingement angle in AWJ machining (milling, turning and drilling) of different materials, such as stainless steel 304, Ti-6-4 on volume removal rate, depth of cut and surface finish are studied. However, attention was not given to kerf geometry and its characteristics. From the literature, it is observed that considerable efforts have been reported on empirical investigation on the influence of various operating parameters, such as water pressure, abrasive mass flow rate and jet feed rate on geometrical characteristics of the JFP. However, there are very limited studies on the dependence of w_t on the a and its modelling. In addition to jet impingement angle, in 2-axis/5-axis milling with AWJs, jet feed rate has considerable influence on the top width of kerf (Hascalik et al., 2007). For AWJ cutting applications, the influence of v on top kerf width is studied (Srinivasu et al, 2009, Niu et al., 1995; Gropetti et al., 1998). Furthermore, the change in the SOD results in generation of corners along the edge of the kerf with specific radius of curvature. The SOD along the JFP varies gradually when the jet impinges at an angle in 5-axis milling (Srinivasu et al., 2009). Hence, the SOD has to be considered in

determining the w_t. Nevertheless, there have been very limited reports on studying the influence of a in the presence of variation in v for AWJ milling applications. For machining (milling, turning and drilling) of different materials, such as stainless steel 304, Ti-6-4 and ceramics, an improved depth of cut ($h(a)$), MRR and surface finish are observed with the change in jet impingement angle (Wang, 2003; Hashish, 1993). However, there are very limited studies that have considered the influence of a on top width of JFP. Although some empirical models exist for prediction of geometrical characteristics of the JFP, they cannot readily be adoptable for AWJ milling as are developed for cutting applications; most of the models in the literature have assumed the top width of kerf is equal to the d_f, which is not true in practice due to the divergence of jet plume (Srinivasu et al., 2009).

From the literature review, it is inferred that the key enabling element for generation of complex geometries in AEMs using AWJ technology is a unified understanding of the influence of the interaction of jet at different feed rates and impingement angles on the JFP generated. Furthermore, there is a need to develop models for prediction of the geometry of the JFP and its dimensional characteristics, such as top width of kerf in 2-axis/5-axis macro/micro milling. In order to address the above issues, in this chapter, the research work done at the University of Nottingham under the NIMRC sponsored research project titled "*Freeform Abrasive WaterJet Machining in Advanced Engineering Materials (Freeform_JET)*", under the following headings was presented: (i) comprehensive investigation on the physical phenomenon involved in the formation of JFP, (ii) development of models for (a) prediction of geometry, and (b) top width, of the JFP.

2. Experimentation and methodology

In order to understand the physical phenomenon involved in generation of the geometry of the JFP at various jet impingement angles and jet feed rates, and to generate the data required to develop models for prediction of JFP geometry and top width, experimental trials were conducted and the complete details are as follows: Milling trials were conducted on 5-axis AWJ (Ormond) cutting system with a streamline SL-V100D ultra-high pressure pump capable of providing a maximum pressure of 413.7 MPa at various mass flow rates (0-1 kg/min) while the jet feed rate can be varied in the range of 0-20,000 mm/min. Garnet (80 mesh size, average Φ180µm - GMA Garnet) abrasive media with sub-angular particle shapes was employed throughout the experimentation to mill SiC ceramic plate (100mmX100mmX10mm). The hardness of the SiC was evaluated as 2500VH. Figure 1a shows a photograph of the experimental setup employed in this study. The structure of the SiC consists of two different regions: α-SiC and β-SiC displaying two different wear characteristics; as α-SiC was reported to have increased strength than β-SiC phase and lower fracture toughness (Lee & Rainforth, 1992), it is expected that the first one will be easier to be removed under AWJ impingement. The two constituents of the SiC ceramic have been revealed by fine diamond polishing (# 6µm/5min followed #1µm/5 min) followed by etching with 'Murakami' (aqueous solution of NaoH and $K_3[Fe(CN_6)]$) solution for 10 minutes. Figure 1b explains the notations used in describing the characteristics of the AWJ process and its erosion outcomes (i.e. kerf shape/dimensions).

As the kerf characteristics are influenced by various operating parameters such as P, d_f, m_f, a, v, SOD and properties of workpiece material, careful consideration has been taken in selecting their values in relation to material of study. Since, SiC is a hard material, a high P of 345 MPa was employed. Furthermore, to maintain the optimum ratio of focusing nozzle diameter to orifice diameter of 3-4 for optimum performance (Chalmers, 1991), a d_f of 1.06 mm and d_o of 0.3 mm were employed. Garnet abrasive of 80 mesh size with an m_f of 0.7 kg/min was employed (Hashish, 1989). SOD of 3 mm was employed as it has been demonstrated that the MRR is insensitive to SOD within the range of 2-5 mm and decreases beyond 5 mm (Hashish, 1987; Laurinat et al., 1993; Ojmertz, 1997). The above operating parameters were kept constant throughout the experimental program. In order to study the influence of v and a on the JFP and its characteristics, the following experimental plan was followed.

- *Examination of the influence of jet feed rate on jet footprint generation*: To understand the influence of jet feed rate on JFP generation, experiments were conducted by varying the v in the range of 100-1700 mm/min in steps of 400 mm/min.

- *Examination of the influence of jet impingement angle on jet footprint generation*: To understand the influence of jet impingement angle on JFP generation, experiments were conducted by varying a in the range of 40^0-90^0 in steps of 10^0. Further, to study the influence of a on kerf geometry at different jet feed rates, cutting trials were performed at different jet impingement angles for smaller ($v = 100$ mm/min) and higher ($v = 900$ mm/min) levels of feed rate.

- *Examination of the influence of number of passes on jet footprint generation*: To understand the influence of number of passes on erosion depth, the contribution of preceding jet pass on the increase in SOD (SOD_{actual}: $SOD_{n+1} = SOD_n + h_n$) and shape of kerf geometry were analyzed. For this purpose, different kerfs were generated by single and double jet passes at $v = 900$ mm/min and $a = 90^0$ at nominal SOD (i.e. 3 mm) and their variation in geometries/characteristics were discussed. Additionally, trials for compensating the increase in SOD at a second jet pass were performed as follows: 1st pass with SOD = 3mm and 2nd pass with a corrected SOD ($SOD_{corrected}$ = SOD-h) have been carried out; where, 'h' represents the erosion depth in single jet pass.
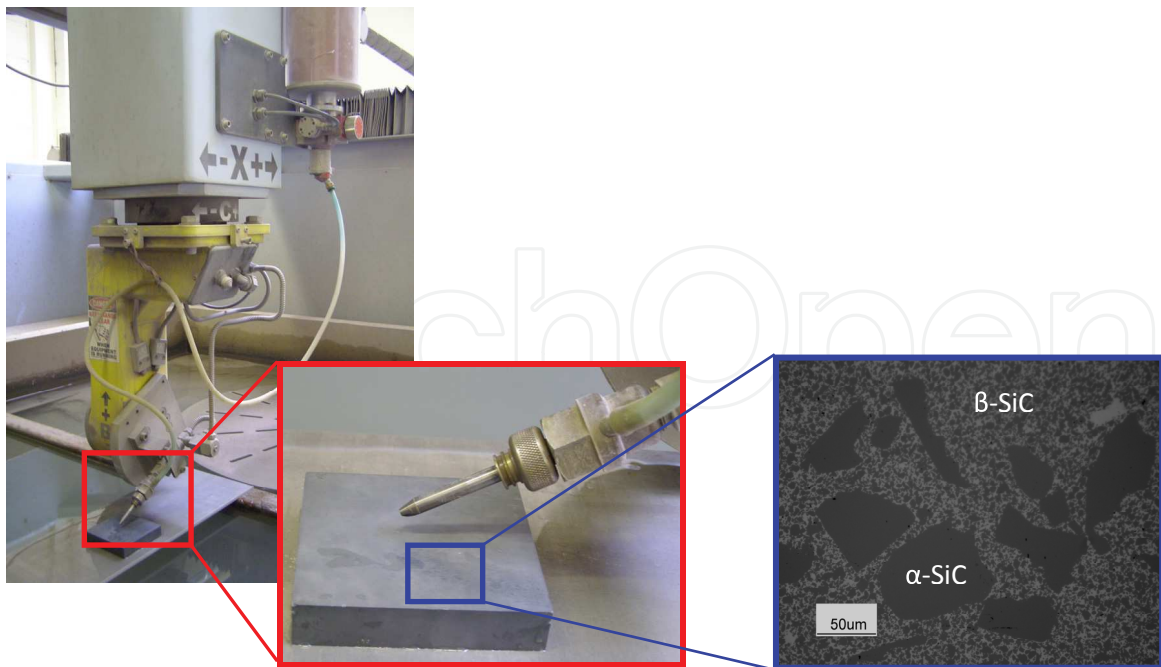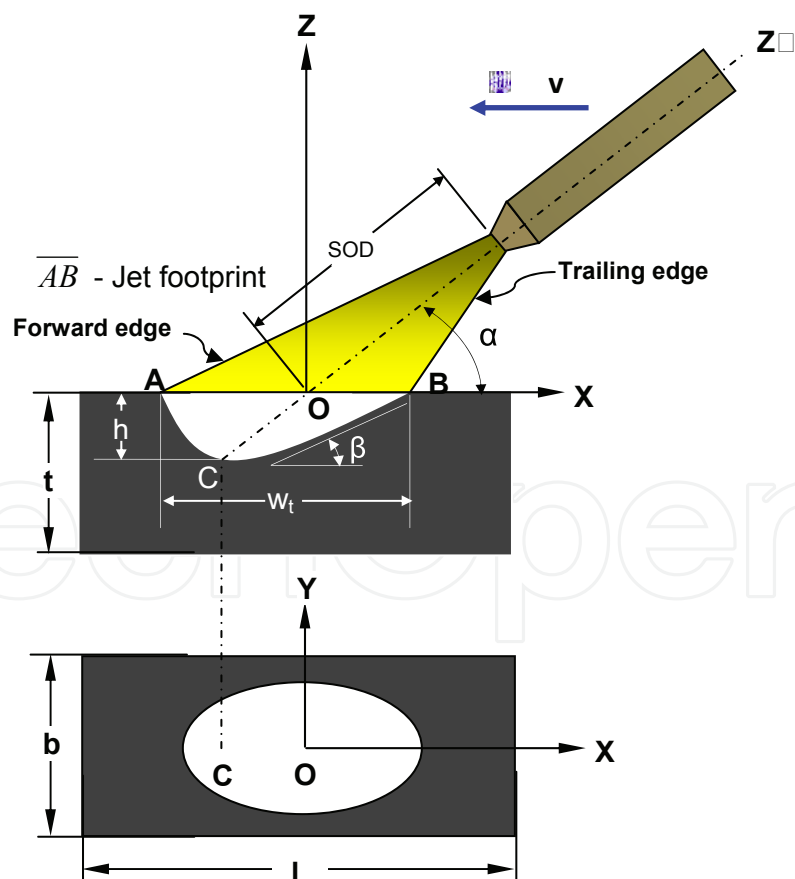
(a)

Fig. 1. (a) Photograph of the experimental setup employed for AWJ machining of SiC ceramic material, (b) Schematic illustration of nomenclature in kerf generation

A summary of the testing program is presented in Table 1. To study the influence of jet impingement angle and jet feed rate on the kerf generation in AWJ machining, the cut surfaces were analysed in two stages (i) geometry of the kerf generated at different jet impingement angles; and (ii) dimensional characteristics of the kerf, such as erosion depth, kerf width, slope of the kerf trailing wall. To enable these investigations, sections across the kerfs have been cut, followed by diamond polishing (# 60μm grit / 10min and 15μm grit / 15min.) to ensure their flatness and to allow accurate measurement of geometry of JFP and its geometrical measurements, such as top width, depth, slope of walls using fibre optic digital microscope (Keyence-VHX) and profilometer. Once the jet footprints were generated they have been 3D scanned (Fig. 4) using a Talysurf CLI 1000 from which the ten kerf profiles were extracted at equal spaced intervals (along jet feed direction) to allow the evaluation of the averaged profiles and their variability at various experimental conditions. The average profiles have then been fed into the geometrical models (developed in MATLAB codes) for their calibration and validation.

Constant operating parameters			
d_f (mm) 1.06	P (MPa) 345	d_o (mm)	0.3
m_f (kg/min) 0.7 (Garnet, 80 mesh)		SOD (mm)	3.0
Variable operating parameters			
S. No.	Objective	Operating parameters	
I	Influence of v on top with of jet footprint	v (mm/min)	100, 500, 900, 1300, 1700
		a (deg)	90
II	Influence of α on top width of jet footprint	v (mm/min)	100, 900
		a (deg)	50, 60, 70, 80 , 90

Table 1. Overview of experimental plan to study the influence of jet impingement angle and jet feed rate on top width of the jet footprint on SiC material

3 Analysis and modelling of abrasive waterjet footprint

3.1 Physical phenomenon involved in the formation of jet footprint
(*Srinivasu et al., 2009*)
Understanding the influence of jet footprint at various impingement angles can be done by analyzing the 2D cross-sectional view of the kerf in the plane of the focusing nozzle/jet tilt. Hence, in the following sections, the variation in 2D geometry of the kerf by considering the key kinematic operating parameters (*a* and *v*) is discussed with the help of schematic illustrations and the experimental results on kerf geometry and dimensional characteristics, such as erosion depth, top kerf width and slope of kerf walls.

3.1.1 Influence of kinematic operating parameters (α and v) on kerf geometry

a) Influence of jet impingement angle on kerf geometry

For better understanding of the kerf generation phenomena at different jet impingement angles, the experimental results are analysed in two distinct situations: (a) normal jet impingement angle ($a = 90^0$) and (b) shallow jet impingement angle ($40^0 < a < 90^0$)

(i) Normal jet impingement (a = 90⁰)

Figure 2a presents the photographs of the kerf cross sectional geometry generated at normal jet impingement angle at various jet feed rates in the range of 100-1700 mm/min while Fig. 2b shows their measured 2D cross-sectional profiles. The geometry of the kerf generated at $a = 90^0$ is symmetric about the vertical axis, which coincides with the jet axis, in this case. The observations are explained with the help of a schematic illustration of jet-material interaction in kerf generation at normal jet impingement (Fig. 3). The kerf geometry is dictated by: (i) jet energy across the jet-material interaction site ($\overline{AB}$); (ii) local impact angles of abrasive particles (θ) across the JFP. Energy of the jet across the jet footprint varies depending on the jet impingement angle (a) and the jet plume divergence, which in turn influences the velocities of water/abrasive particles.

As the exact energy distribution in the jet is not known clearly, uniform (Leber & Junkar, 2003) and Gaussian distributions (Henning & Westkamper, 2003) have been considered by the researchers. On the other hand, by using flow separation technique (Simpson, 1990) and Laser Doppler Anemometry (Chen & Siores, 2003) these distributions are experimentally determined as double slope distribution. Furthermore, it is found that at higher abrasive flow rates and high water pressures, the abrasive flow increases at the core region and decreases towards walls of the focusing nozzle (Simpson, 1990). As higher water pressure and abrasive flow rates were employed in this study, the velocity of water and abrasive particles were assumed to follow the shape of Gaussian distribution. At any cross-section of jet plume (perpendicular to jet axis), velocity profile of water follows nearly Gaussian distribution (Henning & Westkamper, 2003); Yanaida & Ohashi, 1978; Gropetti & Capello, 1992; Kovacevic & Momber, 1995). On the other hand, with the increase in axial distance from the focusing nozzle, the divergence of jet plume increases which in turn cause decrease in axial velocity (Fig. 3). As the velocity distribution in the radial direction of the jet footprint when $a = 90^0$ is symmetric, the erosion energy which is proportional to the velocity (velocity exponent) of water/abrasive particles also follows the same profile. This leads to maximum erosion at centre of jet axis and gradual decrease on either side. At normal jet impingement angle, due to jet plume divergence (Fig. 3), the local impact angle of abrasive particles (θ) with the target surface decreases gradually on either side of the jet axis across the JFP. Thus, the local impact angle varies from $\theta = 90^0$ at centre of jet axis to a critical angle θ_c (where there is no significant erosion of target material) on either side of the JFP. Furthermore, for brittle materials, the maximum erosion is typically observed at normal impact angle ($\theta = 90^0$) and it reduces gradually with the decreasing in θ (Ruff & Wioderborn, 1979). Hence, the comprehensive effect of reduction in (i) velocity of water/abrasive particles (ii) impact angle of abrasive particles, on either side of jet axis contributes to the symmetric nature of the kerf geometry at $a = 90^0$.
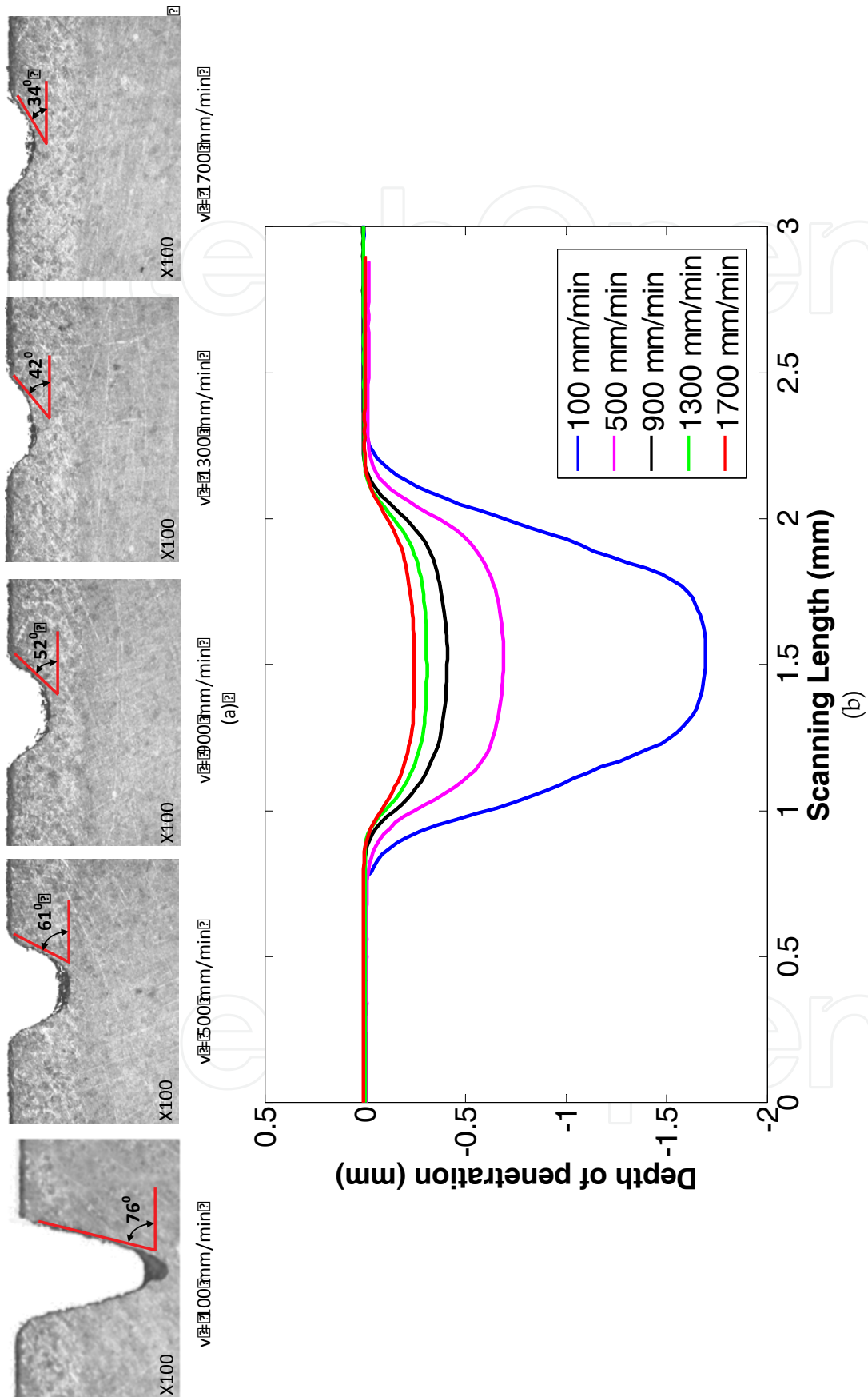
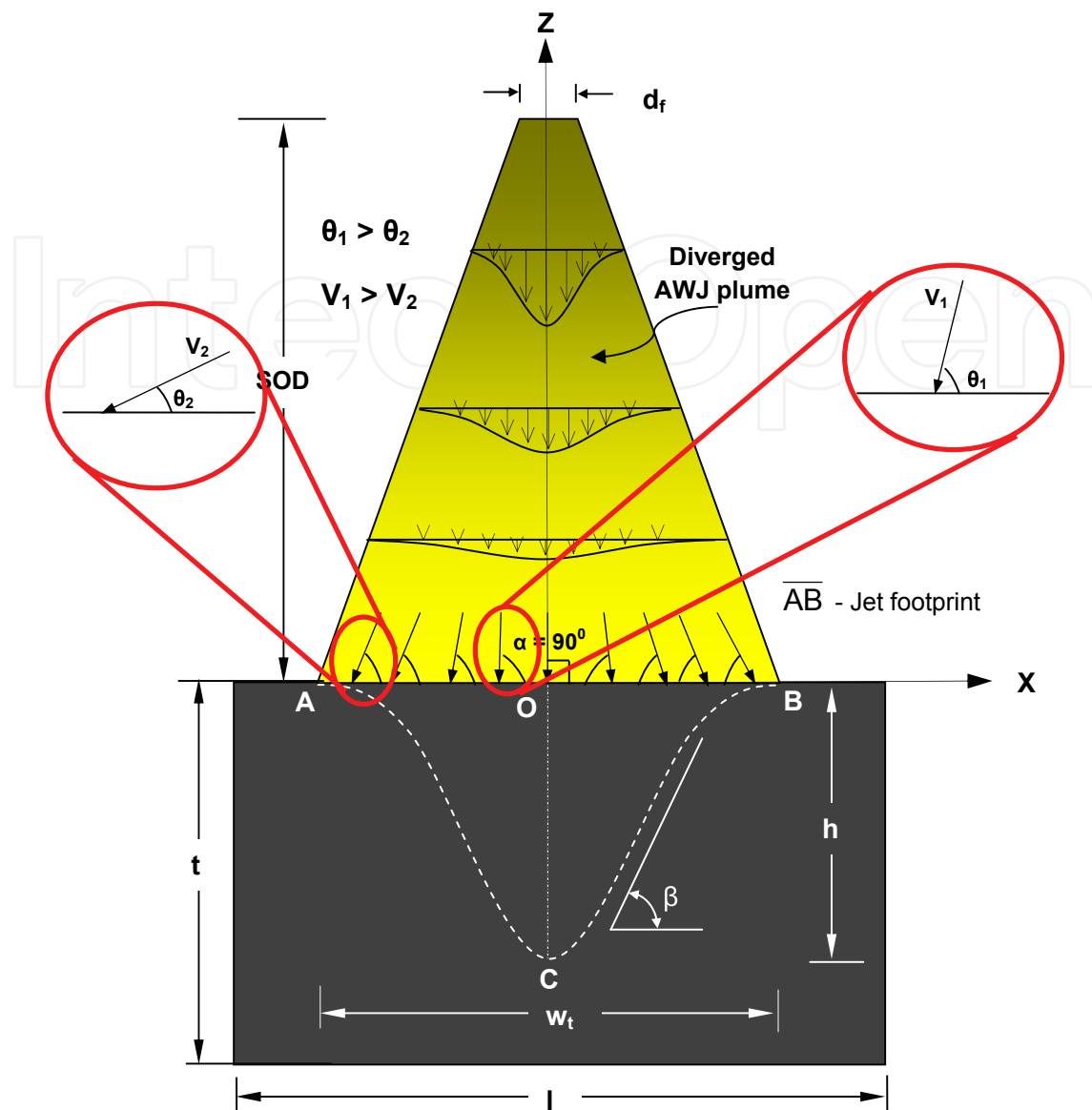Fig. 2. Kerfs generated at different jet feed rates (α = 900) (a) photograph of cross-section, (b) 2D cross-sectional profile.

Fig. 3. Schematic illustration of kerf generation at normal jet impingement angle ($\alpha = 90^0$)

(ii) Shallow angle jet impingement ($40^0 < a < 90^0$)

Figure 4 presents the photographs of kerf cross-sections generated at the different jet impingement angles, i.e. 90^0-40^0, in steps of 10^0 at both lower $v = 100$ mm/min (Fig. 4a (ii)) and higher $v = 900$ mm/min (Fig. 4a (iii)). From Fig. 4, it can be observed that at $\alpha = 90^0$, the kerf geometry is symmetric about the vertical axis (which is the same as the jet axis) as discussed earlier (Fig. 3). However, as the jet impingement angle decreases, the kerf geometry becomes asymmetric. This is explained as follows by the use of Figures 5 and 6 that show the schematic illustration of kerf generation at shallow jet impingement angles. The top view of the kerf gradually transforms from circular (at $\alpha = 90^0$) to elliptical (at $0^0 < a < 90^0$) whereas the side cross-sectional view moves towards the right deviating from the symmetry (Fig. 4(i), Fig. 5).

Furthermore, along the jet footprint ($\overline{AB}$), the erosion depth decreases at a slow rate from 'C' to 'B' and at a fast rate from 'C' to 'A'. These issues can be attributed to: (i) the interaction of various zones of the jet plume which are at varying axial distances from the tip of

focusing nozzle and radial distances from jet axis, at footprint and (ii) variation in 'effective' impact angle of abrasive particles at jet footprint.

With the decrease in jet impingement angle, the width of footprint increases ($\overline{AB} < \overline{A'B'} < \overline{A''B''}$ in Fig. 5) in the direction of $\overrightarrow{XO}$ due to jet plume divergence. However, as a varies in the XZ plane, the increase in the width of JFP in the direction of the XY plane is not significant compared to that on the XZ plane. Hence, the top-view of the kerf gradually transforms from circle (at $a = 90^0$) to an ellipse (at $0^0 < a < 90^0$) with the decrease in a. Maximum erosion depth, $\overline{OC}$ or $\overline{OC'}$ or $\overline{OC''}$, is observed along the jet axis, $\overline{OZ'}$ or $\overline{OZ''}$ or $\overline{OZ'''}$ (Fig. 5). This is due to high velocity of water/abrasive particles along the jet axis. However, the depth decreased rapidly from point 'C' to point 'A' where the forward edge of the jet in the XZ plane meets the target surface (Figures. 5 and 6) and decreases slowly from point 'C' to 'B' where the trailing edge of the jet meets the target surface and that results in asymmetric geometry of kerf. This is explained in the following way: in contrast to normal jet impingement, the footprint on target surface $\overline{A'B'}$ or $\overline{A''B''}$ (Fig. 5) at shallow jet impingement angle occurs at different axial distances (D5 > D4 > D3 > D2 > D1, etc. (Fig. 6) from the tip of the focusing nozzle. As the distance Di increases, the velocity of jet decreases due to jet plume divergence that can be explained with decrease in height of Gaussian profile which in turn causes the decrease in erosive capability of the abrasive particles. The rapid decrease in depth of penetration across the forward part of the footprint ($\overline{OA}$) from 'C' to 'A' can be attributed to the increase in radial distance from jet axis ($\overline{OZ'}$ or $\overline{OZ''}$ or $\overline{OZ'''}$) and the longitudinal distance (D1, D2, D3 D4, D5 etc.), in the direction of the jet axis, across the jet footprint ($\overline{AB}$) from the tip of focusing nozzle. In addition to this, the impact angle of abrasive particles in the direction of footprint $\overrightarrow{OA}$ decreases due to shallower α (Fig. 6). Hence, the cumulative negative influence, i.e. increase in radial and axial distances as well as reduction in impact angle of abrasive particles, results drastic decreases in the velocity of abrasive particles which in turn cause decrease in erosion depth at higher rate towards 'A'. The decreased rate of erosion depth, in the trailing part of the jet footprint ($\overline{OB}$), can be attributed to decrease in axial distance along the jet axis (D2 < D1) and the increase in impact angle of abrasive particles in the direction $\overrightarrow{OB}$. The impact angle of abrasive particles increases gradually in the $\overrightarrow{OB}$ direction that increases the erosion capability of the abrasive particles in brittle materials. Further, the axial distance across the trailing part of the jet footprint ($\overline{OB}$) from the tip of the focusing nozzle decreases which in turn increases the erosion capability of the abrasive particles. However, the increase in radial distance in the direction of $\overrightarrow{OB}$ due to divergence of jet plume reduces the velocity of abrasive particles. Moreover, the divergence along the trailing part of jet plume is geometrically less compared to that in the forward edge of the jet. Hence, the slow rate of decrease in depth of erosion is due to the comprehensive result of positive effect of increase in θ, decrease in axial distance and the negative effect of increase in radial distance from jet axis. The rate of decrease of depth of penetration in forward part and trailing part depends on a. This is in contrast to the case of normal jet impingement where, across the footprint, the distance from the tip of the focusing nozzle is the same (= SOD) which results in symmetric geometry.
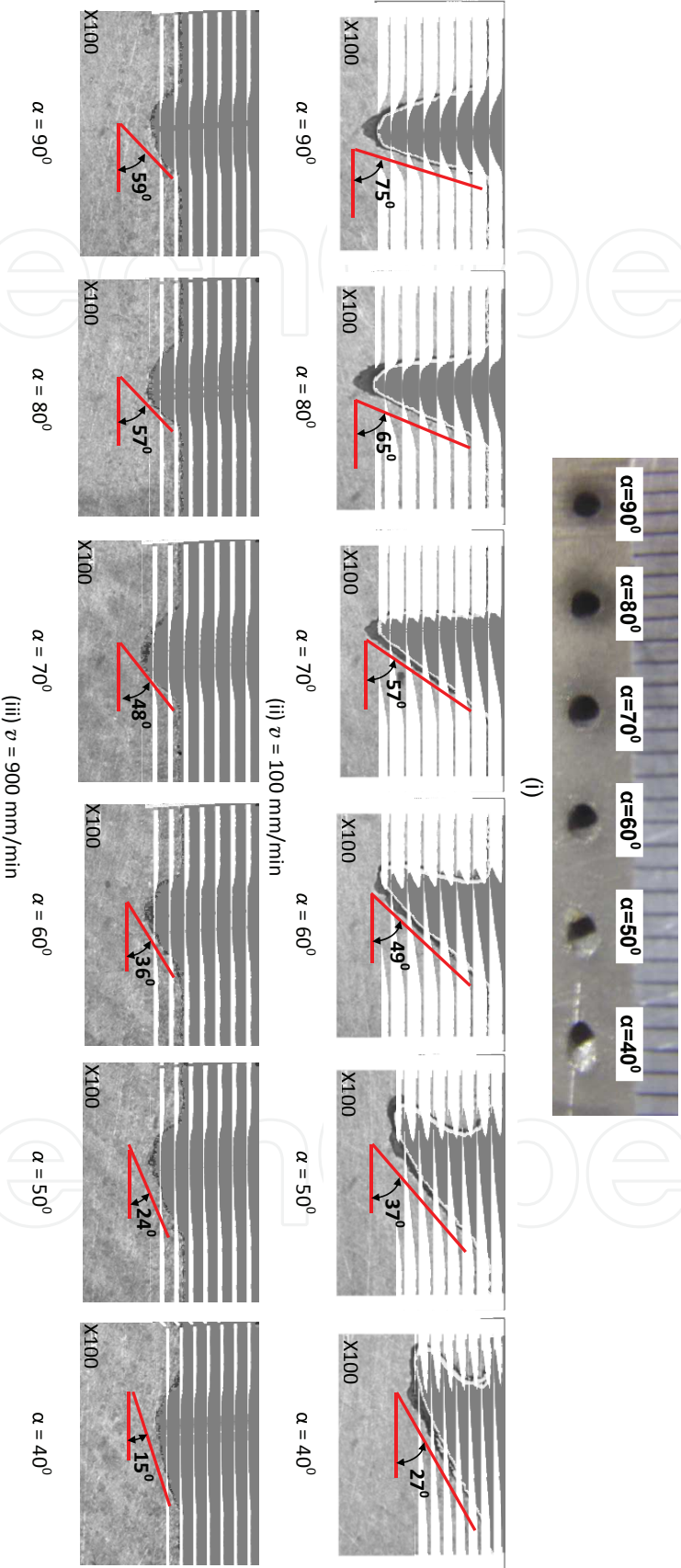
Fig. 4. Photographs of the 3D jet footprints generated at various jet impingement angles ($40^0 < \alpha < 90^0$) (i) top view, and 2D cross sections at (ii) v = 100 mm/min, (iii) v = 900 mm/min

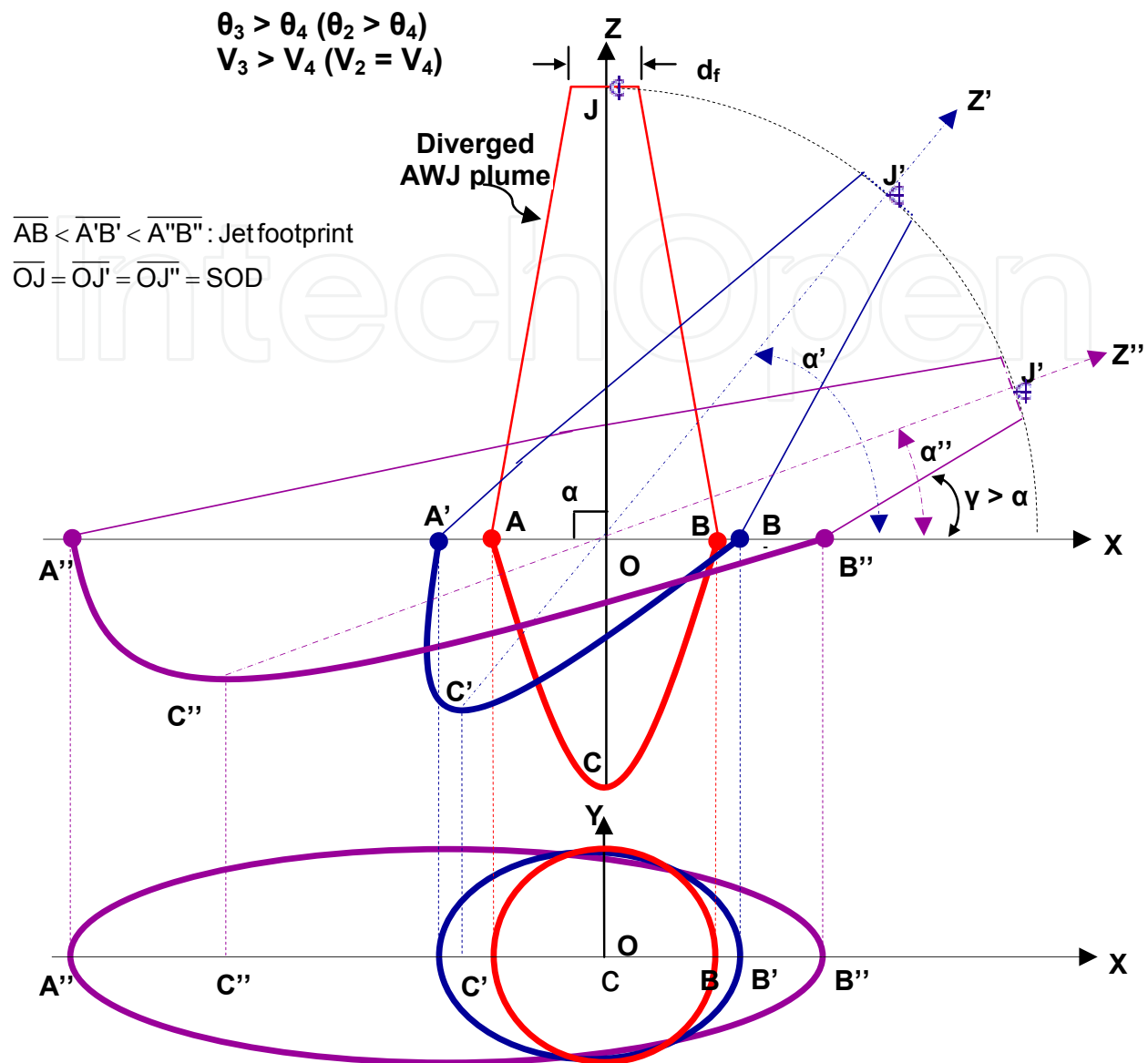Fig. 5. Schematic illustration of variation in jet structure at various jet impingement angles (0 < α < 90⁰) on kerf generation

In addition to the change in geometry, the following changes in dimensional characteristics were observed which influence the geometry of the kerf significantly. From Fig. 4a, it can be observed that the slope of the kerf trailing edge is decreasing with the decrease in *a*. This can be attributed to the shift of jet axis towards the workpiece surface at shallower *a*. In addition to this, with the decrease in α, the depth of erosion was decreased and the top kerf width was increased (Fig. 7) which results in decrease in slope of kerf wall. Further, the slope (*β*) of kerf trailing wall is less than the jet impingement angle (*a*) employed. This can be attributed to the velocity profile that is similar to Gaussian distribution across the jet cross-section. When the jet impinges at a shallow angle, the maximum erosion is along the jet axis $\overline{OZ}'$ (Fig. 6) and the erosion depth in the direction of jet axis across $\overline{OB}$ decreases as the velocity of water/abrasive particle decreases due to its Gaussian nature. This makes the slope of the kerf trailing edge less than the jet impingement angle.
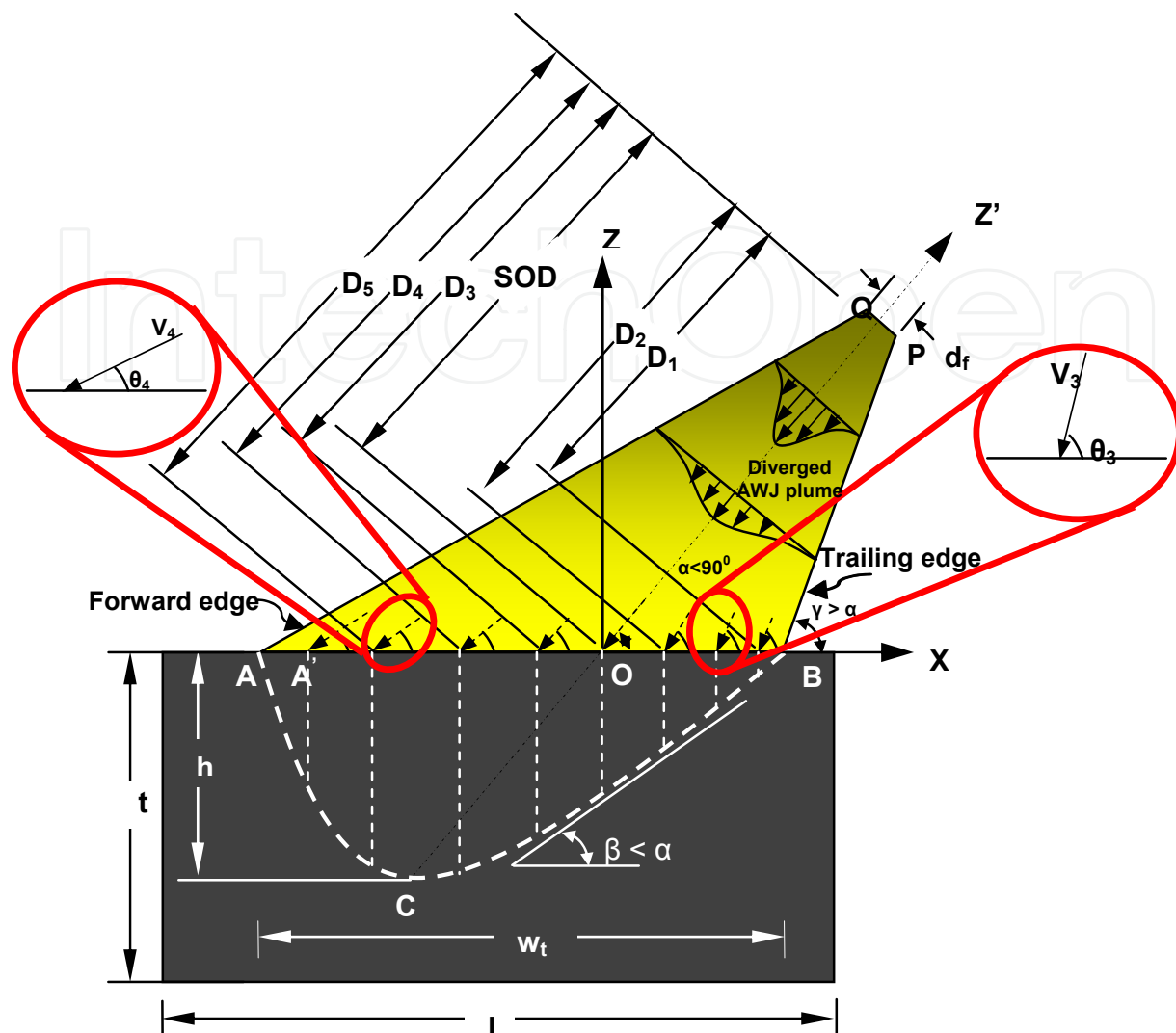
Fig. 6. Schematic illustration of local impact angles of abrasive particles and standoff distance at shallow ($40^0 < a < 90^0$) jet impingement angle on kerf geometry

Maximum erosion depth was observed in the range of 70^0-80^0 jet impingement angle, i.e. for $v = 100$ mm/min erosion is maximum at $a = 80^0$ and $v = 900$ mm/min erosion is maximum at $a = 70^0$ (Fig. 7). This is a slightly different observation compared to the well known observation of maximum erosion at normal impingement ($a = 90^0$) in gas-solid particle erosion for brittle materials (Ruff & Wioderborn, 1979). Similar shift of peak in erosion rate has been reported previously for sodalime glass w11x and WC–Co alloys w12x in certain erosion conditions (Chen et al., 1998; Kim & Park, 1998; Anand et al., 1986; Konig et al., 1988). This can be attributed to the effective average impact angle of abrasive particles and hardness of workpiece (Oka et al., 1997). The effective average impact angle (θ) of particles cannot be 90^0 at $a = 90^0$ and approaches 90^0 at $a < 90^0$. Furthermore, with the increase in hardness, the maximum erosion occurs at higher impact angles. Hence, the shift in maximum erosion was in the range of 70^0-80^0 ($a < 90^0$). The width of the kerf increased with the decrease in a (Fig. 7). This is due to the combined effect of jet impingement angle and jet plume divergence. At lower a, the abrasive particles along the forward edge of the jet plume impinges on workpiece

at a farther distance compared to higher jet impingement angle, due to divergence, which results in increase in width of jet footprint ($\overline{A''B''} > \overline{A'B'} > \overline{AB}$) as was shown in Fig. 5.
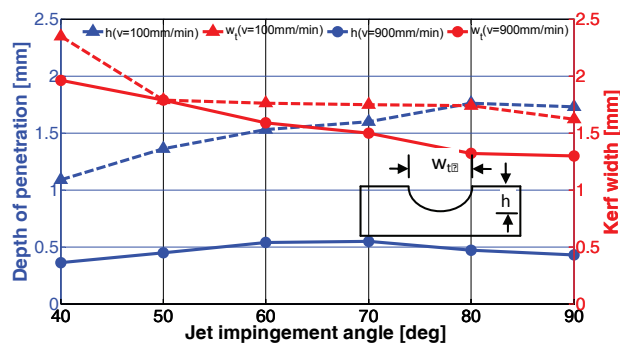

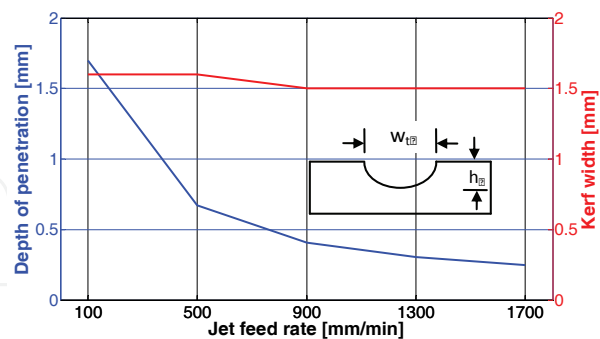Fig. 7. Influence of jet impingement angle ($40^0 < a < 90^0$) on (a) erosion depth and (b) top kerf width

Fig. 8. Influence of jet feed rate ($a = 90^0$) on (a) erosion depth and (b) top kerf width

b) Influence of jet feed rate on kerf geometry
(i) Normal jet impingement (a = 90⁰)

From the Fig. 2a (v = 100-1700 mm/min), it can be observed that the symmetric nature of the kerf geometry is maintained at different v when $a = 90^0$. However, there is a significant variation in the geometry of kerf at different jet feed rates. This can be explained with the change in dimensional characteristics of the kerf geometry, such as depth of penetration (h), top kerf width (w_t) (Fig. 8) and slope of kerf walls (β) (Fig. 2a) with the variation in v. The well known decreasing trend of h with the increase in v can be attributed to the increased exposure time of the material to the jet at lower v (Fig. 8). As the exposure time increases, more abrasive particles participate in erosion and penetrate more into the material which result in increased erosion depth. However, it can be observed that the h is not uniformly increased along the kerf geometry with the decrease in v as the increase in erosion along the kerf corner/walls is smaller than the increase in erosion along jet axis (Fig. 2b). This is explained in the following: As the abrasive particles along the trailing edge of jet plume are at shallower impact angle and the abrasive particles along the jet axis are nearly normal, the scaling of erosion is less for the same time. Furthermore, water/particle velocity along the jet axis is higher than jet plume edges. Moreover, at lower v, at an instantaneous time of 't+1', the abrasive particles interacts with the kerf generated at an instantaneous time 't' which is not a flat surface and cause decrease in 'effective' abrasive particle impact angle from the bottom of the kerf towards the edges of the kerf which results in decreased erosion in this direction. Hence the kerf geometry deviates from the sinusoidal curve and be approximated using simple 'cosine function' approximation. Further, rounding of edges on right side of kerf can be seen from Fig. 4a. This effect was significant at lower feed rates. This may be due to passage of rebounded jet along the left edge ($\overrightarrow{CA}$) of the kerf from the bottom as the jet enters from the left side ($\overrightarrow{BC}$) of the kerf. The kerf width decreased with the increase in jet feed rate, although the difference is insignificant (Fig. 8). This is explained in the following: when a cut is made, at an instantaneous time of 't' sec, the jet footprint, $\overline{AB}$ (Fig. 3), first pass through the material and generates a kerf with top width, which is nearly equal to the width of the JFP. Following that (at infinitesimally small incremental time,

(t+Δt), the jet that has lower width than the footprint (due to divergence of jet plume) passes through the kerf already formed at an instantaneous time of 't' sec and cannot result in any further increase in kerf top width. However, at lower v, the abrasive particles along the boundary of jet, which have low erosion capability, gets enough time to interact with the material and enhance the erosion which results in slight increase in kerf width where these particles cannot make significant erosion at higher v. Hence, a slight decrease in kerf width was observed at higher v (Fig. 8). As a comprehensive view, with the increase in v, the erosion depth of the kerf is decreased and the width of kerf is nearly constant which results in a decrease in the slope of the kerf wall (Fig. 8 and Fig. 4a(i)). The slope of the kerf walls has direct influence on the geometry of the kerf generated. Hence, the jet feed rate plays a significant role in generating the desired kerf geometrical characteristics.

(ii) Shallow angle jet impingement ($40^0 < a < 90^0$)
It can be observed from Fig. 4a that, for the same jet impingement angles, the cross sectional geometry of the kerf generated at higher jet feed rates (v = 900 mm/min) is considerably different in terms of erosion depth, top kerf width and slope of kerf trailing edge from the same generated at lower v (= 100 mm/min). This is also due to the fact, that was observed for normal jet impingement angle at lower v, i.e. interaction of the jet at an instantaneous time of 't+1' on the surface generated at time 't' which is a non-flat surface; and increase in exposure time with the decrease in v. Furthermore, the slope of the kerf trailing wall (β) is decreased at lower v for the same a (Fig. 4a). This can be attributed to the increase in erosion capability of abrasive particles along the jet plume trailing edge $\overline{PQ}$ (Fig. 6) at lower v. The water/abrasive particles have low energy along the trailing edge of diverged jet plume (Fig. 6). At higher v, due to low exposure time of material to the low energy abrasive particles, material cannot be eroded in the direction of jet plume trailing edge $\overline{PQ}$ (Fig. 6). The water/abrasive particles along the jet axis $\overline{OZ'}$, which is less steep than jet plume trailing edge, i.e. $\gamma > a$, are responsible for material removal. Hence, β is smaller. In contrast to this, at lower v, the exposure time of material to the low energy particles increase which enhances the erosion of material in the direction of jet trailing edge which is steeper than jet axis. Hence, at lower jet feed rate, the slope of kerf trailing edge is higher than higher v.

3.1.2 Variation in depth of penetration along jet feed direction

From the bottom of the kerf cross sectional views presented in Figs. 2a and 4a, it is clear that the h along the jet feed direction is not uniform. Figure 9a presents an example of a 3D axonometric plot of the kerf generated at a = 900, P = 345 MPa (= 50,000 psi), v = 500 mm/min and m_f = 0.7 kg/min, where it can be noted the variation in the direction of jet feed. The same behaviour was observed at all jet impingement angles. In order to analyze further, the kerf generated at a = 90^0 was considered. Kerf profiles taken at five equally distanced sections along the jet feed direction are presented in Fig. 9b. Figure 9c presents the errorbar graph (1 standard deviation) of the 3D kerf that presents the variation of kerf profile around the mean profile. From the errorbar graph, it is evaluated that the depth of erosion along the jet feed direction was varying with a standard deviation of 0.015 mm around the mean erosion depth of 0.704 mm. The variation in kerf profile can be attributed to the fluctuations in the pump pressure, jet feed rate employed, abrasive particle mass flow, transverse feed of milling etc. (Hashish, 1989; Oka et al., 1997; Ansari & Hashish, 1993;

Hashish, 1989; Paul et al., 1998). From the previous studies it is observed that the low energy jet (at low P and at higher v levels) generates uniform kerf (Hashish, 1989; Ansari & Hashish, 1993).
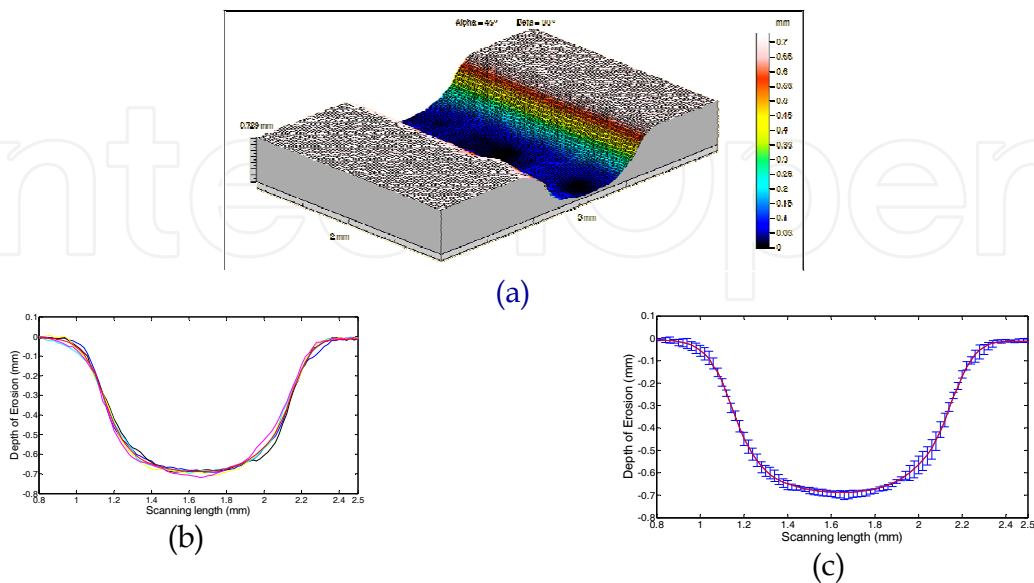

Fig. 9. (a) 3D axonometric plot of kerf generated by AWJ (v=500mm/min), (b) kerf profiles at different regions in the direction of jet feed, (c) Error bar graph of the kerf

3.1.3 Influence of multi-pass on kerf generation

Figure 10 presents the experimental kerf profiles obtained in single (blue profile) and double pass (red profile) operations by keeping all the other operating parameters constant. Intuitively, the double pass is expected to generate the kerf with erosion depth of H ='2xh' (green profile) whereas in reality the generated depth is less than '2xh'.The decrease in depth of penetration in double pass can be attributed to the combined effect of (i) change in local impact angles (θ) of the abrasive particle due to non-flat kerf geometry generated in the first pass and (ii) increase in SOD due to kerf generated in the first pass. The kerf formation in double pass approach is schematically illustrated in Fig. 11. ACB is the kerf geometry generated in single pass with an erosion depth of 'h' and A'C'B' is the kerf geometry generated in double pass operation by considering all the other operating parameters constant.

Influence of kerf geometry generated on the following pass

In a second (or subsequent) pass, erosion is taking place on the previously generated kerf which is a non-flat surface (ACB) (Fig. 11). This differs from a single pass where erosion starts on a flat surface (AB). As explained earlier, at α = 90⁰, the impact angle of the abrasive particles (θ) is 90⁰ on the jet axis ($\overline{OZ}$) and decreases in value on either side of jet axis across the footprint ($\overline{AB}$). However, in erosion by subsequent (e.g. second) passes, the abrasive particles interact with a (non-flat) kerf surface formed in the previous passes. Hence, for subsequent passes, the impact angle of abrasive particles is the angle between the kerf surface formed by the previous passes and abrasive particles impact direction (Fig. 11) which decreases away from the centreline and causes decrease in erosion rate, since erosion is lower at shallower θ for brittle materials.
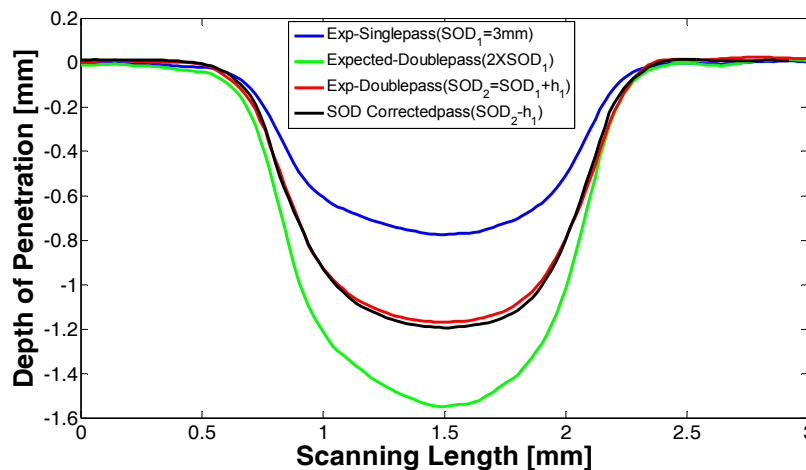
Fig. 10. Influence of number of passes and standoff distance on kerf generation ($\alpha = 90^0$)

b) Influence of SOD on characteristics of kerf generated in double pass

Furthermore, the actual standoff distance (SOD_{actual}) in a second (or subsequent) pass is the sum of SOD set in the first pass and the erosion depth (h), i.e. $SOD_{actual} = SOD + h$. In order to support the intuition experimentally, SOD correction experiments were conducted: 1st pass achieved a maximum penetration depth of 0.45 mm (P = 50,000 PSI, m_f = 0.7 kg/min, v = 500 mm/min, d_f = 1.06 mm, d_o = 0.3 mm, SOD = 3 mm). After the first pass, the SOD becomes 3.45 mm as the depth of penetration achieved in single pass was 0.45 mm, i.e. SOD_{actual} = 3+0.45. Hence, the focusing nozzle was moved down by 0.45 mm which makes the SOD again to 3mm that was employed for a single pass cut. Figure 10 presents the kerf profiles of (a) single pass, (b) intuitive/expected double pass (two folds depth of penetration in single pass cut), (c) experimentally achieved double pass and (d) corrected double pass (cut made after moving down the focusing nozzle by 0.45 mm). All the other operating parameters were kept constant throughout the study. From the results, it can be observed that there is very little change in erosion depth due to the movement of focusing nozzle down by 0.45 mm. However, when the number of passes increases, the small effect of SOD becomes cumulative. From this, it can be concluded that although the increased SOD has influence on the reduction of depth of penetration in following passes, it is not significant. However, it has to be considered for tight dimensional control. Hence, in a comprehensive view, to control the erosion depth in multi-passes, the influence of kerf generated in previous pass and the SOD have to be considered for control over the surface to be generated.

With the knowledge gained from the experimental investigation on the jet footprints, in the following section, development and validation of an analytical model for prediction of JFP at normal jet impingement angle is presented.
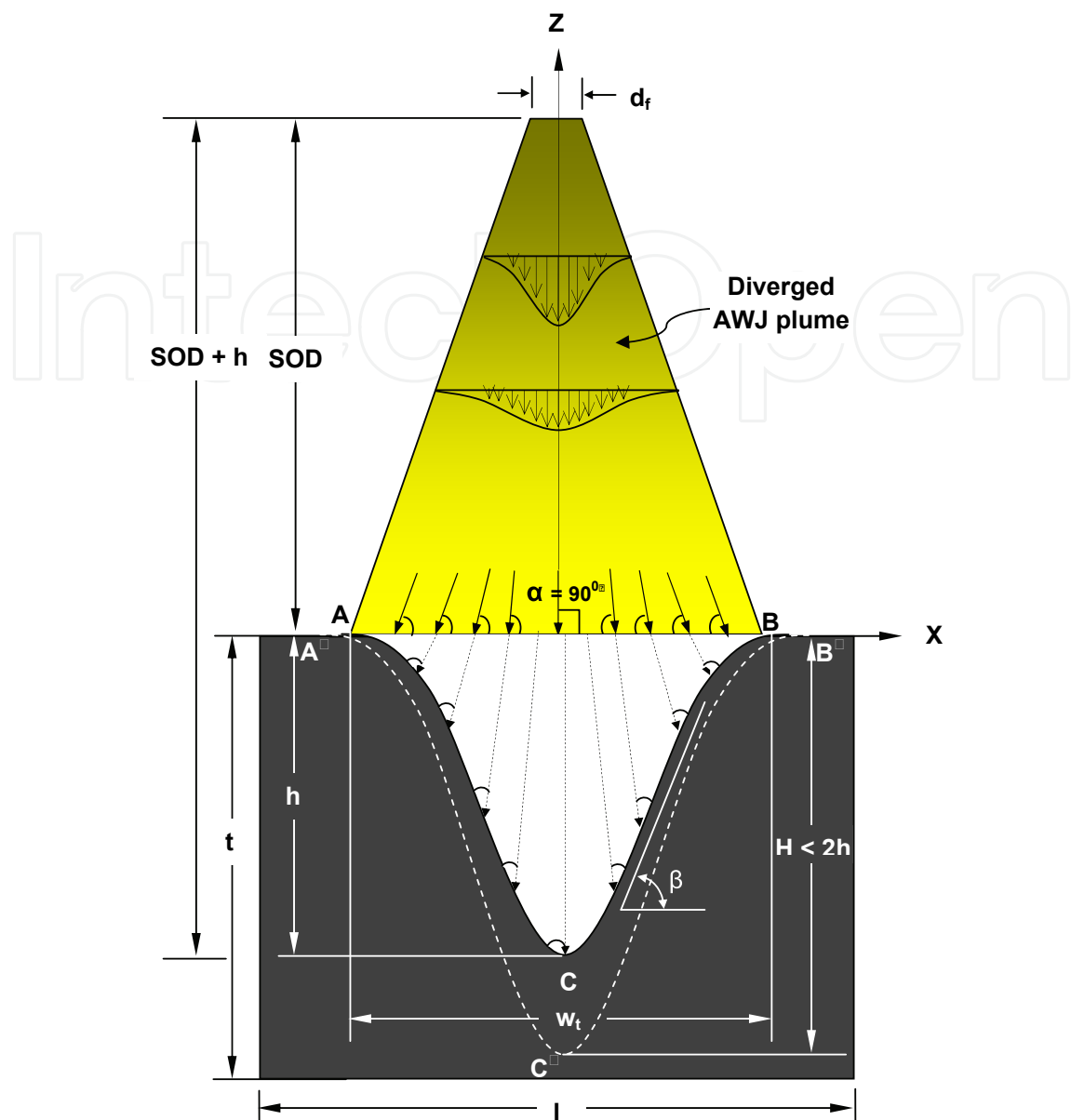
Fig. 11. Schematic illustration of kerf generation in multi-pass operation ($\alpha = 90^0$)

3.2 Model for the jet footprint geometry (*Axinte et al., 2010*)

For this model it was assumed that an abrasive waterjet jet, with radius a, impacts at 90° a flat workpiece surface while moving with a constant feed speed v_f in the y-direction. This means that, for the time being, the proposed model is more applicable to brittle target workpiece materials on which normal jet impingement angle has been found to give higher material removal rates (Hashish, 1993). The jet footprint (Fig. 12a) is a function z= Z(x, y, t) in which x - distance from the jet axis, y - the direction in which the jet moves and t - dwell (exposure) time. For brittle materials, maximum erosion occurs when the jet is perpendicular to the workpiece so this model assumes that the etching rate is proportional to some power (k) of the impingement velocity (Slikkerveer, 1999; Getu et al., 2008; Ghobeity et al., 2008) Eq. (1), of the jet in the direction of the inwards unit normal, Eq. (2), of the surface being etched.
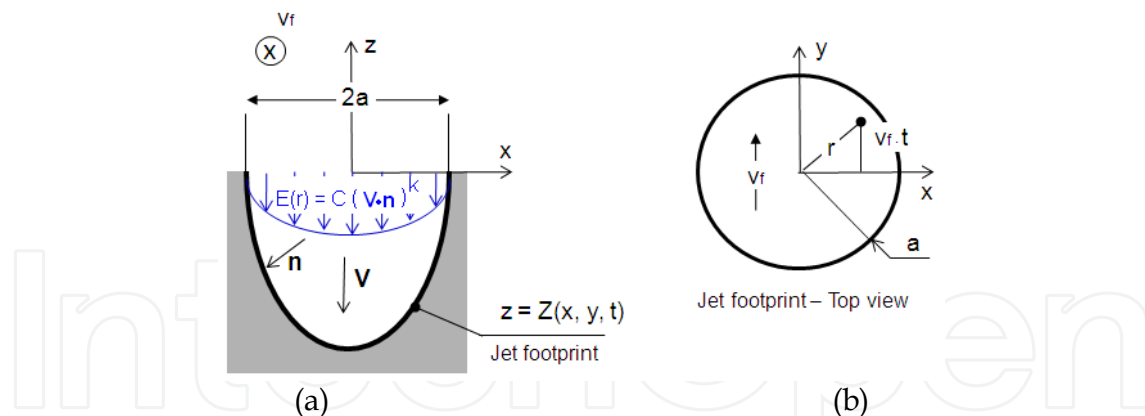
Fig. 12. Schematic of the jet footprint: cross section (a) and top view (b)

$$V = V(r) \begin{pmatrix} 0 \\ 0 \\ -1 \end{pmatrix} \quad \text{where V(r) is the velocity profile of the impinging jet} \quad (1)$$

$$n = \frac{1}{\left(1 + \left(\frac{\partial Z}{\partial x}\right)^2 + \left(\frac{\partial Z}{\partial y}\right)^2\right)^{\frac{1}{2}}} \begin{pmatrix} \frac{\partial Z}{\partial x} \\ \frac{\partial Z}{\partial y} \\ -1 \end{pmatrix} \quad (2)$$

The component of the jet's velocity in the direction of the inwards unit normal of the surface is now given by the dot product of V and n (Slikkerveer, 1999; Getu et al., 2008; Ghobeity et al., 2008; Ten Thije Boonkamp & Jansen, 2002; Hashish, 1993) as shown in Eq. 3. where, n is normal to the kerf surface.

$$V \cdot n = \frac{V(r)}{\left(1 + \left(\frac{\partial Z}{\partial x}\right)^2 + \left(\frac{\partial Z}{\partial y}\right)^2\right)^{\frac{1}{2}}} \quad (3)$$

As the jet moves along the y axis (Fig. 12b), a point situated at distance x from the jet axis (-a $\leq$ x $\leq$ a) will be impinged by the abrasive jet when $-\sqrt{a^2 - x^2} \leq v_f t \leq \sqrt{a^2 - x^2}$ at which times the jet footprint follows Eq. (4).

$$\frac{\partial Z}{\partial t} \propto (V \cdot n)^k \quad (4)$$

Considering that the etching (material specific erosion) rate, E, is dependent only on the radial position r $\leq$ a and defining it as E(r) = C(V·n)^k (Slikkerveer, 1999; Getu et al., 2008; Ghobeity et al., 2008), C and k positive constants, and then substituting Eq. (3), the jet footprint becomes Eq. (5).

$$\frac{\partial Z}{\partial t} = \frac{-E(r)}{\left(1+\left(\frac{\partial Z}{\partial x}\right)^2+\left(\frac{\partial Z}{\partial y}\right)^2\right)^{\frac{k}{2}}} = \begin{cases} \dfrac{-E\left(\sqrt{x^2+v_f^{\,2}t^2}\right)}{\left(1+\left(\frac{\partial Z}{\partial x}\right)^2+\left(\frac{\partial Z}{\partial y}\right)^2\right)^{\frac{k}{2}}} & \text{for} -\sqrt{a^2-x^2} \le v_f t \le \sqrt{a^2-x^2} \\ \\ 0 \ \text{for} -a \le v_f t \le -\sqrt{a^2-x^2} \text{ and } \sqrt{a^2-x^2} \le v_f t \le a \end{cases} \tag{5}$$

As the etching rate E is dependent on the properties of the workpiece material and other process parameters (e.g. pressure, mass flow of abrasives) it is treated as a function that needs to be calibrated using experimental data; note also that for this simple geometry and jet motion, the final surface will be a trench, with no variation in the y-direction. The problem can be made dimensionless by defining: $x = a\bar{x}$; $Z = a\bar{Z}$; $t = \dfrac{a}{v_f}\bar{t}$; $E = \varepsilon v_f \bar{E}$; $y = v_f \bar{t}$;

note that in the following 'barred notations' (e.g. $\bar{x}$) represent dimensionless measures. Here εvf is the maximum etching rate, so that the dimensionless etching rate function $\bar{E}$ has a maximum value of one. In dimensionless terms the geometrical model, Eq. (5), of the kerf becomes as described in Eq. (6).

$$\frac{\partial \bar{Z}}{\partial \bar{t}} = \begin{cases} \dfrac{-\varepsilon \bar{E}\left(\sqrt{\bar{x}^2+\bar{t}^2}\right)}{\left(1+\left(\frac{\partial \bar{Z}}{\partial \bar{x}}\right)^2+\left(\frac{\partial \bar{Z}}{\partial \bar{t}}\right)^2\right)^{\frac{k}{2}}} & \text{for} -\sqrt{1-\bar{x}^2} \le \bar{t} \le \sqrt{1-\bar{x}^2} \\ \\ 0 \ \text{for} -1 \le \bar{t} \le -\sqrt{1-\bar{x}^2} \text{ and } \sqrt{1-\bar{x}^2} \le \bar{t} \le 1 \end{cases} \tag{6}$$

This is a nonlinear partial differential equation, and has no obvious analytical solution. However, if ε is small (obtained at high jet feed speeds), the kerf slope is small and the equation can be linearized Eq. (7).

$$\frac{\partial \bar{Z}}{\partial \bar{t}} = \begin{cases} -\varepsilon \bar{E}\left(\sqrt{\bar{x}^2+\bar{t}^2}\right) & \text{for} -\sqrt{1-\bar{x}^2} \le \bar{t} \le \sqrt{1-\bar{x}^2} \\ \\ 0 \ \text{for} -1 \le \bar{t} \le -\sqrt{1-\bar{x}^2} \text{ and } \sqrt{1-\bar{x}^2} \le \bar{t} \le 1 \end{cases} \quad \text{with } -1 \le \bar{x} \le 1 \tag{7}$$

If now this simple equation is integrated, the shape of the eroded shallow kerf can be obtained as in Eq. (8).

$$\bar{Z}_o(\bar{x}) = -2\varepsilon \int_{\bar{x}}^{1} \frac{\bar{r} \cdot \bar{E}(\bar{r})}{\sqrt{\bar{r}^2+\bar{x}^2}} d\bar{r} \tag{8}$$

After some manipulation, this integral equation can be inverted to obtain Eq. (9).

$$\bar{E}(\bar{r}) = \frac{1}{\varepsilon \pi}\left[\int_{\bar{r}}^{1} \frac{R\left(\bar{Z}_o(R)-\bar{Z}_o(\bar{r})\right)}{\left(R^2-\bar{r}^2\right)^{3/2}} dR - \frac{\bar{Z}_o(\bar{r})}{\sqrt{1-\bar{r}^2}} \right] \tag{9}$$

It is now possible to calibrate the model using an experimentally obtained shallow kerf shape $\overline{Z}_0(\overline{x})$ in Eq. (9) to find the specific etching rate $\overline{E}(\overline{r})$. With $\overline{E}(\overline{r})$ known, the Eq. (6) can be integrated numerically, using Newton method to find $\dfrac{\partial \overline{Z}}{\partial \overline{t}}$ at each time step and ultimately to determine $Z(x)$ for any value of ε, and hence predict the profile of any kerf, including those whose slope is not small (obtained at various jet feed speeds). Therefore, to find the kerf profile at any jet feed speed the following successive steps should be followed:

1. Generate a shallow profile (i.e. $\overline{Z}_0(\overline{x})$) with small kerf slopes.

2. Knowing $\overline{Z}_0(\overline{X})$, the specific etching rate $\overline{E}(\overline{r})$ can be numerically evaluated using Eq. (9).

3. Once $\overline{E}(\overline{r})$ is known, the kerf profile, $Z(x)$, can be obtained for any jet feed speed by solving Eq. (5).

Using process parameters (mf= 0.7 kg/min; P= 345 MPa; D0= 3 mm) mentioned in the previous section at a high value of jet feed speed (vf = 1700 mm/min) a shallow kerf on SiC target workpiece was generated and its scanned profile (i.e. $\overline{Z}_0(\overline{x})$) has been used as calibrated (Fig. 13a) input into Eq. (9) from where employing a MATLAB code the specific etching rate $\overline{E}(\overline{r})$ was evaluated. Then, with $\overline{E}(\overline{r})$ known, predictions of the kerf profiles for smaller jet feed speeds (vf = 100, 500, 900 and 1300 mm/min) have been generated and compared with those experimentally obtained; this revealed that only for small jet feed speed (i.e. vf = 100 mm/min), the model predicts noticeably deeper (approx. 30 μm) kerf than the experimental one (see Model 1 – Fig. 13e). This is somehow an expected finding since with deeper kerf profiles, the real stand-off distance (D) increases considerably (40%) with the increase of jet dwell time (decrease of vf). Therefore, the bottom of the kerf is situated at larger values of stand-off distance from the jet nozzle and consequently less erosion than the theoretical one occurs here. To account for this phenomenon, it has been thought that the distance between the jet and the workpiece should be included in the model.

If D0 is the initial SOD between the centre of the nozzle and the point (x, z) = (0, 0), then the distance from the opening of the jet to any point on the kerf surface is given by D(x, t) = D0 − Z(x, t). Preliminary experimental trials on SiC target workpiece showed that the maximum jet penetration occurs at a stand-off distance of 3 mm but if the jet is any closer then cracks or breaks may occur on the target surface. This suggests that:

$$\frac{\partial Z}{\partial t} \propto F\big(D(x,t)\big) \tag{10}$$

where F is the linear function F(D(x, t)) = 1 − b·[D(x, t) − 3], and b ≥ 0 should be determined by fitting the model to experimental data. Combining this with Eq. (4), the new kerf profile dependence it is obtained, Eq. (11).

$$\frac{\partial Z}{\partial t} \propto \frac{- E(r) \cdot F\big(D(x,t)\big)}{\left(1 + \left(\dfrac{\partial Z}{\partial x}\right)^2 + \left(\dfrac{\partial Z}{\partial y}\right)^2\right)^{\frac{k}{2}}} \tag{11}$$

Hence, after applying the same non-dimensionalization procedure, Eq. (6) now becomes the corrected jet footprint dependence as shown in Eq. (12).

$$\frac{\partial \bar{Z}}{\partial \bar{t}} = \begin{cases} \dfrac{-\varepsilon \bar{E}\left(\sqrt{\bar{x}^2 + \bar{t}^2}\right) \cdot F\left(D(\bar{x},\bar{t})\right)}{\left[1 + \left(\dfrac{\partial \bar{Z}}{\partial \bar{x}}\right)^2 + \left(\dfrac{\partial \bar{Z}}{\partial \bar{t}}\right)^2\right]^{\frac{k}{2}}} & \text{for } -\sqrt{1-\bar{x}^2} \le \bar{t} \le \sqrt{1-\bar{x}^2} \\[4mm] 0 & \text{for } -1 \le \bar{t} \le -\sqrt{1-\bar{x}^2} \text{ and } \sqrt{1-\bar{x}^2} \le \bar{t} \le 1 \end{cases}$$
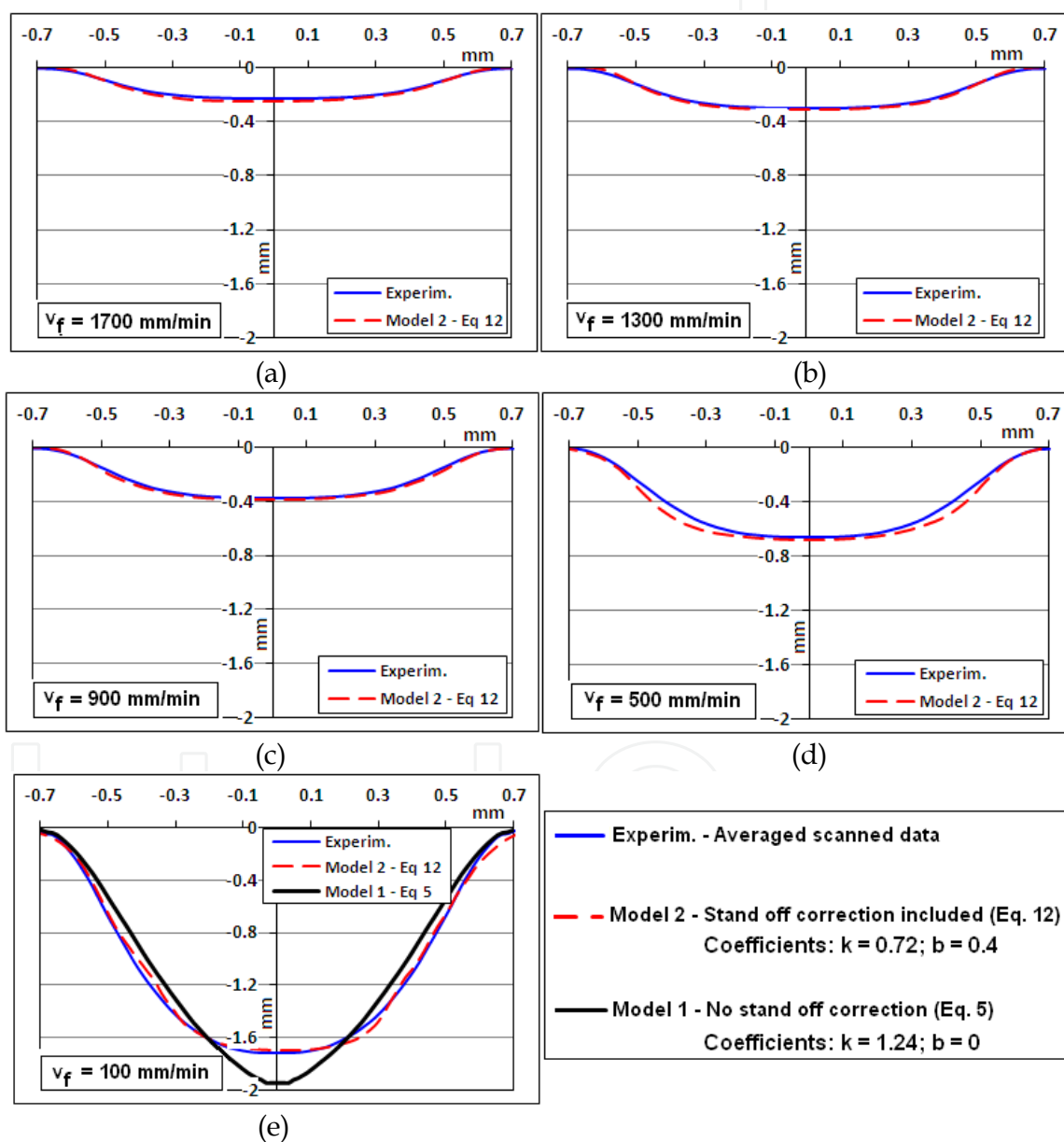
(12)

Fig. 13. Experimental vs. predicted kerfs at various jet feed speeds

This can again be solved as before by linearizing the problem which approximates D(x, t) = D0 when vf is large (vf= 1700 mm/min). Therefore, F(D(x, t)) is just a constant and $\overline{E}(\overline{r})$ is the same as in Eq. (9). Utilising the same calibration method as before and the corrected jet footprint model, Eq. (12), the comparison between the predicted (modelled) kerf profiles and the experimental data is presented in Fig. 13 where the notations Model 1 and Model 2 refer to footprint mathematical predictions on which the correction of stand-off distance was omitted (Eq. (5) for k=1.24) and included (Eq. (12) for k=0.72, b=0.4) respectively. The summarised results in Fig. 13 clearly show that the corrected jet footprint model is capable to predict at high degree of accuracy (error <5%) the kerf profile at various jet feed speeds.

The model presented, in this section, can only approximate the geometry of the JFP and cannot effectively predict the jet footprint's top width, which is one of the critical parameters in controlling the dimensions of the final component milled as mentioned in earlier sections. Hence, in the following section, a model developed exclusively for prediction of top width of the JFP is presented.

3.3 Model for top width of jet footprint (*Srinivasu, D.S. & Axinte, D.A.*)

3.3.1 Development of model for top width of jet footprint

In 2-axis machining, the top width (w_t) of the JFP can be determined by considering the diameter of focusing nozzle (d_f), jet plume divergence in air (φ) and SOD. The development of model for the w_t of the JFP involves two stages: Firstly, an expression for the jet plume divergence (φ) at normal jet impingement angle is derived by considering the d_f, SOD and the w_t generated at a jet feed rate of 1700mm/min. Secondly, an expressions for the $w_t(a)$ at shallow jet impingement angles is derived based on the geometry of the tilted structure of the jet plume at shallow a (Fig. 14b), by considering the previously evaluated φ.

a) Expression for jet plume divergence, φ

The jet plume diverges in air with an angle of φ after emerging from the focusing nozzle of bore diameter, d_f, before interacting with the target workpiece situated at a distance of SOD (Fig. 14a). Due to the divergence of the jet plume at normal jet impingement angle, the width of the jet increases gradually from d_f (at the tip of focusing nozzle) to w_t (at a distance of SOD) depending on the jet plume divergence angle. The expression for the φ can be derived as follows:

From Δ^{le} AEC (Fig. 14a), $$\varphi = \tan^{-1}\left(\frac{w_t - d_f}{2(SOD)}\right) \tag{13}$$

b) Expression for width of jet footprint at normal jet impingement, w_t

The top width of the JFP at a distance x, at normal jet impingement, can be approximated by the width (diameter) of jet plume at that distance (Fig. 14a). As the width of the jet depends on the distance between workpiece and the tip of focusing nozzle, initial diameter of focusing nozzle and jet plume divergence, the w_t can be derived as follows:

From Δ^{le} MNC (Fig. 14a), w_t at a distance of $X = d_x = d_f + 2(\overline{MN}) = d_x = d_f + 2 x \tan(\varphi)$ (14)

c) Expression for width of jet footprint at shallow jet impingement, w_t (a)

The jet plume divergence angle is constant and will not change with the change in jet impingement angles. Hence, at shallower jet impingement angles ($a < 90^0$), the width of the JFP can be approximated geometrically from the consistent structure of the jet plume as the summation of three parts on the target workpiece surface (Fig. 14b): (i) leading part of the top width of JFP generated by leading portion of jet plume (a - $\overline{A'E'}$), (ii) right part of the top width of JFP generated by trailing portion of jet plume (b - $\overline{F'B'}$) and (iii) middle part generated by the diameter of focusing nozzle ($\overline{E'O'}$ + $\overline{O'F'}$).

$$w_t(a) = \overline{A'B'} = \overline{A'E'} + \overline{E'O'} + \overline{O'F'} + \overline{F'B'} \tag{15}$$

Evaluation of $\overline{A'E'}$: (a)

From Δ^{le} C'A'E' (Fig. 14b), $\overline{A'E'} = \left(SOD + \dfrac{d_f}{2\tan(\alpha)} \right) \dfrac{\sin(\varphi)}{\sin(\alpha - \varphi)}$ (15.1)

Evaluation of $\overline{E'O'}$:

From Δ^{le} J'E'O' (Fig. 14b), $\overline{E'O'} = \dfrac{d_f}{2\sin(\alpha)}$ (15.2)

Evaluation of $\overline{O'F'}$:

From Δ^{le} I'O'F'(Fig. 14b), $\overline{O'F'} = \dfrac{\overline{I'F'}}{\sin(\alpha)} = \dfrac{d_f}{2\sin(\alpha)}$ (15.3)

Evaluation of $\overline{F'B'}$:(b)

From Δ^{le} D'F'B' (Fig. 14b), $\overline{F'B'} = \overline{F'D'}\dfrac{\sin(\varphi)}{\sin(\alpha + \varphi)} = \left(SOD - \dfrac{d_f}{2\tan(\alpha)} \right)\dfrac{\sin(\varphi)}{\sin(\alpha - \varphi)}$ (15.4)

Finally, from Eq. (3.1), Eq. (3.2), Eq. (3.3) and Eq. (3.4)

$$w_t(a) = \overline{A'B'} = \overline{A'E'} + \overline{E'O'} + \overline{O'F'} + \overline{F'B'}$$
$$= \left(SOD + \dfrac{d_f}{2\tan(\alpha)} \right)\dfrac{\sin(\varphi)}{\sin(\alpha - \varphi)} + \dfrac{d_f}{\sin(\alpha)} + \left(SOD - \dfrac{d_f}{2\tan(\alpha)} \right)\dfrac{\sin(\varphi)}{\sin(\alpha + \varphi)} \tag{16}$$
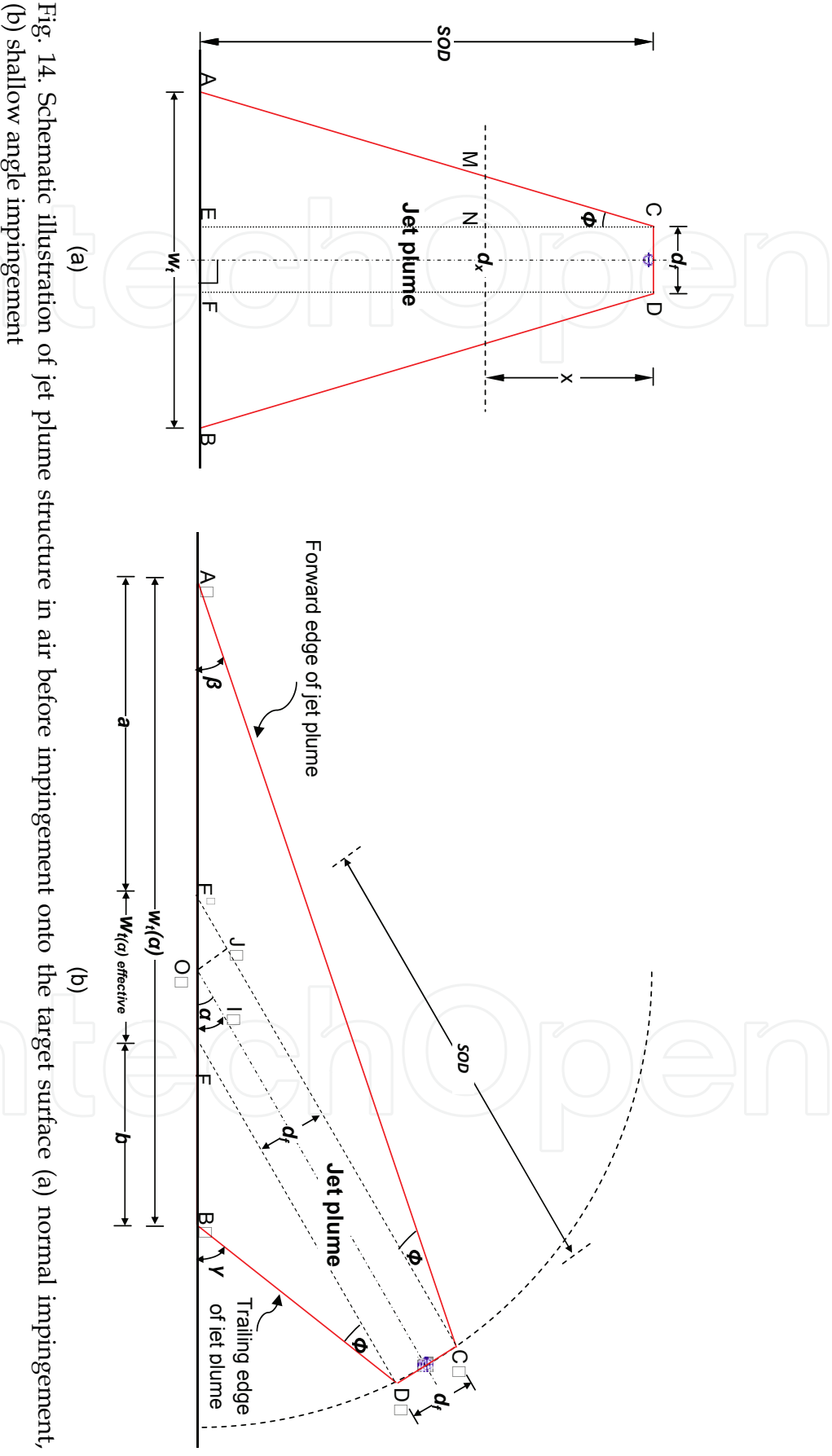
Fig. 14. Schematic illustration of jet plume structure in air before impingement onto the target surface (a) normal impingement, (b) shallow angle impingement

However, this model cannot be employed at jet feed rates higher than 100 mm/min as the effective divergence of jet plume, that is responsible for erosion, decreases at higher jet feed rates, although the jet plume divergence angle does not change with v as discussed earlier. Hence, the prediction of $w_t(a)$ at desired jet feed rates, higher than 100 mm/min, needs the evaluation of φ at that desired v, and is termed in this modelling study as effective divergence angle, φ_v. The φ_v replaces the jet plume divergence angle (φ) in the above model for evaluation of top width of JFP at any jet impingement angle at desired v.

3.3.2 Assessment of the proposed model for the top width of jet footprint

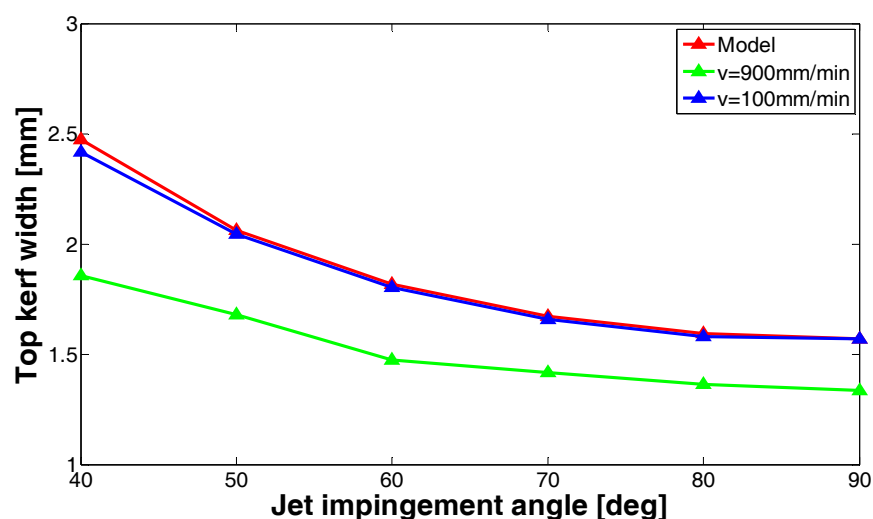*a) Without considering the 'effective jet plume divergence'*

Fig. 15. Variation in top width of jet footprint with the jet impingement angle without considering the 'effective jet plume divergence'

Figure 15 presents the w_t predicted by the proposed model without considering the parameter: *'effective jet plume divergence'*, along with the experimentally achieved values at lower (v = 100mm/min) and higher (v = 900mm/min) jet feed rates. The predicted values are in well agreement with the experimental values at v = 100 mm/min. However, the difference is considerable at higher jet feed rate (v = 900 mm/min). Furthermore, this difference increased at shallower jet impingement angles. This may be explained as follows:

(i) With the increase in v, the exposure time of the material to the jet plume decreases. Furthermore, the erosion capability of the abrasive particles along the jet plume edges is less due to low impact angle of abrasive particles (Fig. 6 and Fig. 3). Because of the combined effect of exposure time and low impact angle, the erosion capability of the abrasive particles along the jet plume edges decreases with the increase in jet feed rate. Hence, the *'effective jet plume divergence'* is, indirectly, a function of jet feed rate. However, the proposed model evaluated the erosion at higher jet feed rate (v = 900mm/min) according to the jet plume divergence angle (φ) that was evaluated at lower jet feed rate (v = 100mm/min) which results in increase in difference between predicted and experimental values.

(ii) On the other hand, as the a decreases, the width of spray region at jet-material interaction site increases which cannot generate considerable erosion due to lower impact angle of abrasive particles and lesser velocity of water along the forward edge of the jet plume ($\overline{A'C'}$ - Fig. 6). However, in this region, the model assumes considerable erosion, according to geometrical structure of the jet plume divergence, without considering the influence of abrasive particle impact angle. Hence, there is significant difference between predicted and experimental w_t.

Hence, in the following section, the model is modified by including the influence of jet feed rate by a parameter called *'effective jet plume divergence'*, φ_v, to improve its predictive capability at any v.

b) Considering the 'effective jet plume divergence', φ_v

Figure 16a and 16b presents the top width of the JFP predicted by the proposed model with the consideration of the influence of jet feed rate with the introduction of the parameter - *'effective jet plume divergence'* φ_v, along with the experimental results at lower (100mm/min) and higher (900mm/min) v. The difference between the predicted and experimental w_t values at higher jet feed rate was reduced significantly compared to the earlier case. This can be attributed to the inclusion of φ_v parameter that has taken care of the reduction in effective jet plume divergence at higher jet feed rates. For this purpose, φ evaluated at desired jet feed rate (v = 900 mm/min), i.e. φ_v, which is 3^0, was substituted in the model (Eq. 16) and becomes Eq. 16'.

$$w_t(\alpha) = \left(SOD + \frac{d_f}{2\tan(\alpha)} \right) \frac{\sin(\varphi_v)}{\sin(\alpha - \varphi_v)} + \frac{d_f}{\sin(\alpha)} + \left(SOD - \frac{d_f}{2\tan(\alpha)} \right) \frac{\sin(\varphi_v)}{\sin(\alpha + \varphi_v)} \qquad (16')$$

The reduction in effective jet plume divergence can be observed as it is reduced from 5.24^0 at lower jet feed rate ($\varphi_{v=100\,mm/min}$) to 3^0 at higher v ($\varphi_{v=900\,mm/min}$).

Although, the predicted w_t of the JFP at different jet impingement angles is in well agreement with the experimental values, there exists an error at shallower jet impingement angles (Fig. 16). Furthermore, this error increased at higher jet impingement angles and higher v (= 900 mm/min) (Fig. 16b). This can be explained as follows: Figure 2b presents the schematic illustration of the variation in leading ($\overline{A'E'}$ - caused by the leading edge - $\overline{A'C'}$) and trailing ($\overline{F'B'}$ - caused by the trailing edge - $\overline{D'B'}$) parts of w_t at shallow a. Figure 17 present the trends of variation in $\overline{A'E'}$´ (Eq. 3.1) and $\overline{F'B'}$´ (Eq. 3.2) at different jet impingement angles according to the proposed model. Although, the length of the leading and trailing parts of the JFP increases with the decrease in a, the rate at which $\overline{A'E'}$ increases is higher (Fig. 17). This is due to the fact that the increased distance of points on the target surface from the tip of focusing nozzle along the forward part is higher than the trailing part and is responsible for the error in prediction by the model. At larger SOD, the jet structure becomes very unstable and do not follow exactly the variation as assumed in

the modelling. However, the model assumes considerable erosion at this point. Hence, the actual jet plume divergence that was evaluated at desired v cannot be applied exactly and differs slightly at higher distances from the tip of focusing nozzle and this is the case that arises at shallower jet impingement angles. This leads to the over prediction of top width of JFP by the proposed model at shallower jet impingement angles.

Furthermore, as discussed earlier, at shallower a, the particles along the leading edge ($\overline{A'C'}$) of the diverged plume cannot initiate considerable erosion due to shallower particle impact angles and is also not stable (Fig. 6). The scale of erosion reduces further at higher jet feed rates as the exposure time of the workpiece material to the abrasive particles reduces. Hence, the combined effect of unstable portion of the jet along the edges of the plume at larger distances, smaller impact angles along jet plume edges contribute to the error. Finally, the error can also be attributed to the non consideration of (i) quantitative measure of erosion caused at different impact angles of the abrasive particles and (ii) the erosion capability of the deflected jet from the target surface.
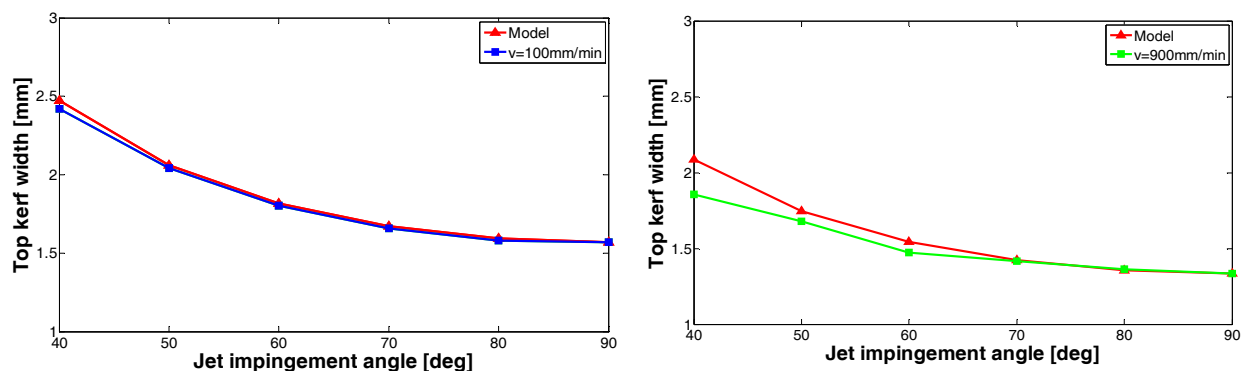

Fig. 16. Variation of top width of jet footprint with the jet impingement angle by considering the effective jet plume divergence (a) φv=100 mm/min = 5.24^0, (b) φv=90^0 mm/min = 3^0
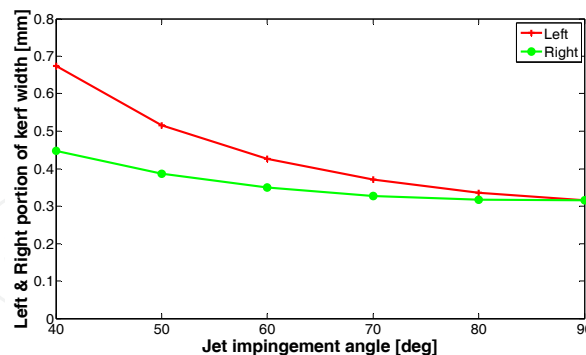

Fig. 17. Variation of leading (A'E') and trailing (F'B') portions of the top width of jet footprint at different jet impingement angles by the proposed model

4. Conclusions

Jet footprint (JFP) is the building block in fabrication of complex shaped components by 2-axis/5-axis abrasive waterjet milling in which the jet feed rate and impact angle are varied continuously according to the shape to be produced. Hence, in this chapter, the research work done at the University of Nottingham under the NIMRC sponsored research project

titled "*Freeform Abrasive WaterJet Machining in Advanced Materials* (Freeform_JET)", under the following headings: (i) investigations on the physical phenomenon involved on the formation of JFP, (ii) development of models for prediction of geometry of JFP, and (iii) development of model for top width of the JFP were presented. The findings of this research work was summarised as follows:

4.1 Physical phenomenon involved in generation of JFP

For the first time, a detailed analysis of the geometry of the JFP by considering the key kinematic operating parameters (jet impingement angle, jet feed rate) on abrasive waterjet machining of advanced engineered SiC ceramic, which is difficult to machine with conventional approaches due to its high hardness and low fracture toughness, is presented. In-depth analysis of the mechanism of kerf geometry formation under the influence of key kinematic operating parameters of AWJ: emphasizing the dependence of JFP on both jet impingement angle and erosion time (given by jet feed rate), the variation in the geometry of the kerf was explained, with the help of schematic illustrations and dimensional characteristics obtained from experiments, based on two key elements: (i) variation of axial distance from tip of focusing nozzle and radial distance from jet axis, and (ii) impact angle of the individual abrasive particles across JFP. While the variation of impact angle of individual abrasives across the JFP accounts for the "cosine type" symmetrical kerf at normal jet impingement angles, the variation of SOD and divergence of jet plume, when jet impinges at shallower angles, are the main factors in obtaining asymmetrical kerf geometries. Amplitudes of these non/symmetrical kerf geometries are very much dependent on the jet exposure time (jet feed rate) due to increase in erosion along jet axis and erosion capability of abrasive particles at shallower impact angle. At 90^0 jet impingement angle, as the effect of local impact angle of abrasives is cumulative, with the decrease of the jet feed rate, the symmetrical kerfs become more elongated along their axis and therefore simple cosine function approximation is less appropriate for their geometry. Further, the kerf generated at shallower jet impingement angles cannot be approximated by simple 'cosine function' approximation.

Relationship between the key kinematic parameters of AWJ and dimensional characteristics of kerf: The influence of *a* and *v* on dimensional characteristics, such as depth of penetration, top kerf width, slopes of kerf walls was analyzed. Maximum erosion depth was observed at jet impingement angle in the range of 70^0–80^0 as the effective average impact angle of abrasive particles approaches 90^0 in this range and also this shift can be attributed to the material hardness. In contrast to nearly constant width at normal jet impingement, an increase in width was observed at a shallower jet impingement angle which is due to the increase in width of jet footprint.

Study of the influence of successive AWJ passes on the "resultant" kerf geometry: Careful analysis of the kerf amplitude (penetration) along jet impingement axis showed that once a footprint is generated after the first jet pass, the next one "inherits" a non-flat target surface that indirectly leads to change in local standoff distances and impact angles of abrasives that ultimately results in lesser erosion on the lateral walls of the kerfs. Based on these aspects, an in-depth analysis of the kerf geometry after two consecutive jet passes has shown that real jet penetration does not follow a pure factorial rule (penetration depth number of

passes); this observation is of key importance for generating multi-pass AWJ milled surfaces at controlled depth. Apart from investigating the dependencies between the kinematic parameters of AWJ machining with the geometrical and dimensional characteristics of the jet footprint, this work flags-up to the machining community the technical challenges to be addressed when proposing machining strategies for milling complex geometry surfaces.

4.2 Analytical model for prediction o f the geometry of the JFP

A geometrical model was developed that enables the prediction of the geometry of the JFP for maskless controlled-depth AWJ milling when the jet impinges normally on target workpiece. The model relies on a nonlinear partial differential equation in which a specific response (etching rate) of the workpiece material to the waterjet conditions is included. By taking limiting conditions (i.e. high jet feed speeds) on the proposed geometrical model, shallow kerf profiles are generated that enable the calibration/identification of the specific etching rate of the workpiece materials to be identified. Then, knowing this key characteristic of the jet-workpiece interaction, the full geometry of the jet footprint can be obtained for any (technologically required) jet feed speed by employing numerical methods to solve the non-linear differential equation which the proposed model is based on. An example of model validation was presented for 90° jet impingement angle against a SiC ceramic as target material, on which, the specific etching rate was determined (at constant m_f= 0.7 kg/min; P= 345 MPa) by the use of analytical models first, to which a scanned shallow kerf profile, obtained for high jet feed (v_f= 1700 mm/min), was input. Then, the JFP at various jet feed speeds (v_f= 100, 500, 900, 1300 mm/min) were obtained and compared with the experimental ones. This revealed that only at low values of jet feed speeds (high jet dwell times) the predicted kerf profile was deeper (by 30 µm) than the real ones; however, the gradient of the kerf was found to be very similar. This finding revealed the need to introduce into the model a linear correction on the SOD of the nozzle to the real target surface that develops as eroded kerf profile. Such addition to the geometrical model enabled accurate (errors < 5%) prediction of the JFP over a wide range of jet feed speed values. The proposed geometrical JFP model, initially developed for normal jet impingement angle, finds its use in developing innovative jet paths capable to generate complex geometry surfaces by continuously altering the jet feed speed in such a way that the succession of JFPs can envelope the desired AWJ milled surface.

4.3 Analytical model for prediction of top width of jet footprint

In this section, the physical phenomenon involved in formation of the top width of the JFP at various jet impingement angles was analysed and the model for the top width was developed by considering the jet impingement angle, jet plume divergence, SOD and jet feed rate. The findings of this work are as follows:

- *Physical phenomena involved in generation of top width*: The change in the cross-section of the jet plume, parallel to the surface of the target workpiece, with the orientation of the jet dictates the shape of the JFP generated and its geometrical characteristics. The jet plume cross-section at the machining zone is nearly circular in shape at the normal jet impingement and gradually transforms to elliptical with the decrease in jet impingement angles. Hence, the top width of the footprint is the diameter of the circle at normal impingement and is length of major axis at shallower jet impingement

angles. The top width of the JFP generated is influenced by the diameter of focusing nozzle, jet plume divergence in air and SOD.

- *Edge quality*: The edge quality of the kerf deteriorated with the increase in jet feed rate at normal jet impingement. At shallower jet impingement angles, chipping is significant along the leading edges of the JFP due to unstable nature of the part of the forward portion of the jet plume.

- *Top width variation*: An increasing trend of the top width of the JFP was observed with the (i) decrease in jet impingement angle, and (ii) decrease in jet feed rates. For the same jet impingement angle, the top width of the JFP is decreased with the increase in jet feed rate. The influence of jet feed rate is considered in the model by a parameter defined as 'effective jet plume divergence'.

- *Assessment of the model predictions*: The inclusion of the 'effective jet plume divergence' parameter into the model has enabled the prediction of top width of JFP at any jet feed rates. The current model does a correct prediction at lower jet feed rates if the divergence of the water jet is taken into account, however, it over predicts at higher velocities and smaller jet impingement angles because the effect of particle velocity variation along top width of JFP and impingement angle on the abrasion rate is not taken into account.

Although the deflected jet is capable of doing secondary machining and influences the characteristics of the JFP, this aspect was not considered in the above models to avoid mathematical complications. Furthermore, these models have not included the effect of particle impact angle on the erosion. By taking into consideration, the effect of abrasive particle impact angle, erosion theories and the secondary machining by the deflected jet plume, the predictive capability of the models in prediction of JFP geometry, top width can be improved further at shallower impact angles. In addition to considering the above aspects, the researchers are developing models for prediction of JFPs at shallower jet impingement angles and resulting kerfs at various degrees of overlap, which are the building blocks in generation of complex shaped parts in advanced engineering materials.

5. References

Ahmet Hascalik; Ulas Caydas & Hakan Gurun (2007). Effect of traverse speed on abrasive waterjet of Ti–6Al–4V alloy, *Materials and Design*, 28, 1953-1957.

Anand, K.; Morrison, C.; Scattergood, R.O.; Conrad, H.; Routbort, J.L. & Warren, R. (1986). Erosion of multi phase materials, in: Institute of Physics Conference Series, Adam Higler, London, pp. 949–961.

Andrews, D.R. & Horsfield, N. (1983). Particle collisions in the vicinity of an eroding surface, Journal of Physics D: *Applied Physics*, vol. 16, pp. 525-538.

Ansari, A.I. & Hashish, M. (1993). Volume removal trends in abrasive water jets, Transactions of ASME, *Manufacturing Science and Engineering*, 64, 629-641.

Axinte, D.A.; Srinivasu, D.S.; Billingham, J. & Cooper, M. (2010). Geometrical modelling of abrasive waterjet footprints: a study for 90º jet impact angle, *Annals of CIRP - Manufacturing Technology*, 59, 341-346.

Chalmers, E.J. (1991). Effect of parameter selection on abrasive waterjet performance, in *Proceedings of 6th American Waterjet Conference*, Houston, Texas, pp. 345-354.

Chen, F.L. & Siores, E. (2003). The effect of cutting jet variation in surface striation formation in abrasive waterjet cutting, *Journal of Materials Processing Technology*, 135, 1-5.

Chen, L.; Siores, E. & Wong, W.C.K. (1996). Kerf characteristics in abrasive waterjet cutting of ceramic materials, *International Journal of Machine Tools and Manufacture*, 36(11), 1201-1206.

Chen, L.; Siores, E. & Wong, W.C.K. (1998). Optimising abrasive waterjet cutting of ceramic materials, *Journal of Materials Processing Technology*, 74, 251–254.

Freist, B; Haferkamp, H; Laurinat, A. & Louis, H. (1989). Abrasive waterjet machining of ceramic products, in: *Proceedings of 5th American Waterjet Conference*, Toronto, Canada, pp. 191-204.

Gropetti, R. & Capello, E. (1992). On an energetic semi-empirical model of hydro-abrasive jet material removal mechanism for control and optimization in: *Proceedings of 11th International Conference on Jet Cutting Technology*, St-Andrews, Scotland, pp. 101-122.

Groppetti, R; Gutema, T & Dilucchio, A. (1998). A contribution to the analysis of some kerf quality attributes for precision abrasive waterjet cutting, in *14th International Conference on Jet Cutting Technology*, Belgium, pp. 253-269.

Gudimetla, P.; Wang, J. & Wong, W. (2002). Kerf formation analysis in the abrasive waterjet cutting of industrial ceramics, *Journal of Material Processing Technology*, 128(1-3), 123-129.

Hashish, M. (1987). Milling with abrasive waterjets: A preliminary investigation, in *Proceedings of 4th U.S. Waterjet Conference*, Berkeley, C.A., pp. 1-10.

Hashish, M. (1989). An investigation of milling with abrasive waterjet, Transactions of ASME, *Journal of Engineering for Industry*, 111, 158-166.

Hashish, M. (1989). Machining of advanced composites with abrasive waterjets, *Manufacturing Review*, 2(2), 142-150.

Hashish, M. (1993). The effect of beam angle in abrasive waterjet machining, Transactions of ASME, *Journal of Engineering for Industry*, 115, 51–56.

Henning, A. & Westkamper, E. (2003). Modelling of wear mechanisms at the abrasive waterjet cutting front, in: *Proceedings of WJTA American Waterjet Conference*, Houston, Texas, USA, pp. Paper 3-A.

Hocheng, H. & Chang, K.R. (1994). Material removal analysis in abrasive waterjet cutting of ceramic plates, *Journal of Materials Processing Technology*, 40(3-4), 287-304.

Inasaki, I. (1987) Grinding of hard and brittle materials, *Annals of the CIRP- Manufacturing Technology*, 36, 463-471.

Kahlmana, L.; Öjmertz, K.M.C. & Falk, L.K.L. (2001). Abrasive-waterjet testing of thermo-mechanical wear of ceramics, *Wear*, 248, 16–28.

Kim, J.J. & Park, S.K. (1998). Solid particle erosion of SiC and SiC–TiB composite hot-pressed with Y2 O3, *Wear*, 222, 114–119.

Konig, W.; Dauw, D.F.; Levy, G. & Panten, U. (1988). EDM-future steps towards the machining of ceramics, *Annals of CIRP - Manufacturing Technology*, 37, 623–631.

Kovacevic, R. & Momber, A.W. (1995). Statistical character of the failure of multiphase materials due to high pressure waterjet impingement, *International Journal of Fracture*, 71, 1-14.

Laurinat, A.; Louis, H. & Wiechert, G. M. (1993). A model for milling with abrasive water jets, *Proceedings of 7th American Water Jet Conference*, Seattle, Washington, pp. 119-139.

Lebar, A. & Junkar, M. (2003). Simulation of abrasive waterjet machining based on unit event features, Proceedings of Institution of Mechanical Engineering-Part B: *Journal of Engineering Manufacture*, 217(B5), 699 - 703.

Lee, W.E. & Rainforth, W.M. (1992). Ceramics Microstructures: property control and processing. London: Chapman & Hall.

Miller, D.S. (2004). Micromachining with abrasive waterjets, *Journal of Materials Processing Technology*, 149, 37–42.

Momber, A.W. & Kovacevic, R. (2003). Hydro abrasive erosion of refractory ceramics, *Journal of Materials Science*, 38, 2861-2874.

Momber, A.W.; Eusch, I. & Kovacevic, R. (1996). Machining refractory ceramics with abrasive water jets, *Journal of Materials Science*, 31(24), 6485-6493.

Niu, M.S.; Kobayashi, R. & Yamaguchi, T. (1995). Kerf width in abrasive waterjet machining, in *Proceedings of 4th Pacific Rim Interenational Conference on Waterjet Technology*, Shimizu, Japan.

Ojmertz, K.M.C. & Amini, N. (1994). A discrete approach to the abrasive waterjet milling process, *Proceedings of 12th International Conference on Jet Cutting Technology*, pp. 425-434.

Ojmertz, K.M.C. (1997). *A study on abrasive waterjet milling*, Ph.D. Thesis, Chalmers University of Technology.

Oka, Y.I.; Ohnogi, H.; Hosokawa, T. & Matsumura, M. (1997). The impact angle dependence of erosion damage caused by solid particle impact, *Wear*, 203-204, 573-579.

Paul, S.; Hoogstrate, A.M.; van Luttervelt, C.A. & Kals, H.J.J. (1998). An experimental investigation of rectangular pocket milling with abrasive water jet, *Journal of Material Processing Technology*, 73, 179 -188.

Richerson, D.W. (2006). Modern Ceramic Engineering: properties, processing and use in design: CRC, Taylor Francis.

Ruff, A.W. & Wioderborn, S.W. (1979). Erosion by solid particle impact, in: Treatise on Material Science and Technology: Erosion, New York., pp. 69-126.

Samant, A.N. & Dahotre, N.B. (2009). Laser machining of structural ceramics - A review, Journal of European Ceramic Society, 40(3-4), 287-304.

Shipway, P.H. & Hutchings, I.M. (1993). Influence of nozzle roughness on conditions in a gas blast erosion rig, *Wear*, vol. 162-164, pp. 148-158.

Shipway, P.H. (1997). The effect of plume divergence on the spatial distribution and magnitude of wear in gas-blast erosion, *Wear*, Vol. 205, 169-177.

Simpson, M. (1990). Abrasive Particle Study in High Pressure Water jet Cutting, *International Journal of Water Jet Technology*, 1, 17-28.

Siores, E.; Wong, W.C.K.; Chen, L. & Wager, J.G. (1996). Enhancing abrasive waterjet cutting of ceramics by head oscillation techniques, *Annals of CIRP - Manufacturing Technology*, 45(1), 327-330

Srinivasu, D.S. & Axinte, D.A. (in press). An analytical model for top width of jet footprint in abrasive waterjet milling: a case study on SiC ceramics, *Proceedings of the Institution of Mechanical Engineers, Part B: Journal of Engineering Manufacture*.

Srinivasu, D.S.; Axinte, D.A.; Shipway, P.H. & Folkes, J. (2009). Influence of kinematic operating parameters on kerf geometry in abrasive waterjet machining of silicon carbide ceramics, *International Journal of Machine Tools & Manufacture*.

Tuersley, I.P.; Jawaid, A. & Pashby, I.R. (1994). Review: Various methods of machining advanced ceramic materials, *Journal of Materials Processing Technology*, 42(4), 377-390.

Wang, J. (2003). The Effects of the Jet Impact Angle on the Cutting Performance in AWJ Machining of Alumina Ceramics, Key Engineering Materials, *Advances in Abrasive Technology* V, vol. 238-239, 117-122.

Yanaida, K. & Ohashi, A. (1978). Flow characteristics of water jets in air, in: 4th *International Symposium on Jet Cutting Technology*, pp. A3-39.

Zeng, J. & Kim, T.J. (1996). An erosion model of polycrystalline ceramics in abrasive waterjet cutting, *Wear*, 193, 207-217.

Zeng, J.; Munoz, J. & Kain, I. (1997). Milling ceramics with abrasive waterjets – An experimental investigation, in: *Proceedings of 9th American Waterjet Conference*, Dearborn, Michigan, pp. 93-107.
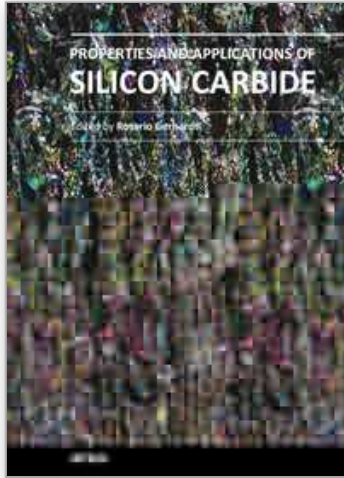
Properties and Applications of Silicon Carbide

Edited by Prof. Rosario Gerhardt

In this book, we explore an eclectic mix of articles that highlight some new potential applications of SiC and different ways to achieve specific properties. Some articles describe well-established processing methods, while others highlight phase equilibria or machining methods. A resurgence of interest in the structural arena is evident, while new ways to utilize the interesting electromagnetic properties of SiC continue to increase.

How to reference

In order to correctly reference this scholarly work, feel free to copy and paste the following:

S. Srinivasu D. and A. Axinte D. (2011). Investigations on Jet Footprint Geometry and its Characteristics for Complex Shape Machining With Abrasive Waterjets in Silicon Carbide Ceramic Material, Properties and Applications of Silicon Carbide, Prof. Rosario Gerhardt (Ed.), ISBN: 978-953-307-201-2, InTech, Available from: http://www.intechopen.com/books/properties-and-applications-of-silicon-carbide/investigations-on-jet-footprint-geometry-and-its-characteristics-for-complex-shape-machining-with-ab

INTECH
open science | open minds